The important roles of surface tension and growth rate in the contribution of new particle formation (NPF) to cloud condensation nuclei (CCN) number concentration: evidence from field measurements in southern China

Mingfu Cai[1,2,3,4], Baoling Liang[3], Qibin Sun[3], Li Liu[4], Bin Yuan[1,2*], Min Shao[1,2], Shan Huang[1,2], Yuwen Peng[1,2], Zelong Wang[1,2], Haobo Tan[4], Fei Li[4,6], Hanbin Xu[3], Duohong Chen[7], and Jun Zhao[3,5,8*]

[1] Institute for Environmental and Climate Research, Jinan University, Guangzhou, Guangdong 511443, China

[2] Guangdong-Hongkong-Macau Joint Laboratory of Collaborative Innovation for Environmental Quality, Guangzhou, Guangdong 511443, China

[3] School of Atmospheric Sciences, Guangdong Province Key Laboratory for Climate Change and Natural Disaster Studies, and Institute of Earth Climate and Environment System, Sun Yat-sen University, Zhuhai, Guangdong 519082, China

[4] Institute of Tropical and Marine Meteorology/Guangdong Provincial Key Laboratory of Regional Numerical Weather Prediction, CMA, Guangzhou 510640, China

[5] Southern Marine Science and Engineering Guangdong Laboratory (Zhuhai), Zhuhai, Guangdong 519082, China

[6] Laboratory of straits meteorology, Xiamen, Guangdong 361012, China

[7] Guangdong Environmental Monitoring Center, Guangzhou 510308, China

[8] Guangdong Provincial Observation and Research Station for Climate Environment and Air Quality Change in the Pearl River Estuary, Guangzhou, Guangdong 510275, China

*Corresponding authors: Bin Yuan (byuan@jnu.edu.cn) and Jun Zhao (zhaojun23@mail.sysu.edu.cn)

Abstract.

The contribution of new particle formation (NPF) to cloud condensation nuclei (CCN) number concentration varies largely under different environments, and dependsdepending on several key factors such as formation rate (J), growth rate (GR), distribution of preexisting particles and properties of new particles during NPF events. This study investigatesinvestigated the contribution of NPF to the N_{CCN} and its controlling factors based on measurements conducted at the Heshan supersite, in the Pearl River Delta (PRD) region of China during fall-time 2019. The size-resolved cloud condensation nuclei activity and size-resolved particle hygroscopicity were measured by a cloud condensation nuclei counter (CCNc) and a hygroscopic tandem differential mobility analyzer (HTDMA), respectively, along with a scanning mobility particle sizer (SMPS) and a diethylene glycol scanning mobility particle sizer (DEG-SMPS) for particle number size distribution (PNSD). A typical NPF event on 29th October was chosen to investigate the contribution of the NPF to N_{CCN} under several supersaturation ratios. Two particle properties (hygroscopicity and surface tension) affect CCN activation with the latter being more important in terms of the CCN concentration (N_{CCN}). A lower value of surface tension (i.e., 0.06 N m^{-1}) than pure water assumption (0.073 N m^{-1}) could increase the N_{CCN} at SS=1.0% by about 20% during non-event period and by about 40% during the event. In addition, an earlier peak time corresponding to a lower critical diameter (D_{50}) was also observed. The results show that high formation rate, growth rate, and low background particle concentration lead to high number concentrations of newly-formed particles. The high growth rate was found to have the most significantprofound impact on the N_{CCN} which can be attributed to the factfacts that a higher growth rate can grow particles to the CCN size in a shorter time before they are scavenged by pre-existing particles. Two other NPF events (an event on 18th October in this campaign and an event on 12th

December, 2014 in Panyu) were chosen to perform sensitivity tests under different scenarios (growth rate, formation rate, and background particle concertation). The calculated N_{CCN} at SS=1.0% on 12th December, 2014 was significantly lower than that from the other two events. The event on 12th December was re-simulated using high growth rate taken from the event on 18th October which resulted in similar CCN concentrations between the two events (12th December and 18th October), implying that the growth rate is the major impact factor~~most controlling factor~~ for CCN activation. Our results highlight the importance of growth rate and surface tension when evaluating the contribution of NPF to the N_{CCN}.

1 Introduction

Atmospheric particles have direct effects on global climate by adsorbing and scattering solar radiation, while they can act as cloud condensation nuclei (CCN) and exert influences on cloud formation, life cycle, and albedo, hence indirectly affect the global radiation balance. In general, atmospheric particles have a cooling effect on the global climate with the highest uncertainty among all the climatic forcings (Stocker et al., 2013). The relationship between the CCN number concentration (N_{CCN}) and its climatic effect represents one of the major uncertainties.~~In general, atmospheric particles have a cooling effect on the global climate, although the highest uncertainty exists on their climatic contribution among all the climatic forcings (Stocker et al., 2013). The relationship between the CCN number concentration (N_{CCN}) and its climatic effect represents one of the major uncertainties and challenges in evaluating the aerosol climatic effect.~~ It is hence essential to carry out field measurements to investigate the CCN activity and its major impact factor~~controlling factors~~.

New particle formation (NPF) as an important source of global atmospheric particles, is frequently

observed in various atmospheric environments, including forest, urban, marine, and agricultural regions (Kulmala et al., 2004). Once formed, the particles can grow to the CCN sizes (50-100 nm) within a few hours and contribute significantly to the N_{CCN} (Leng et al., 2014; Spracklen et al., 2008; Dameto de España et al., 2017). The extent to which newly-formed particles can contribute to the N_{CCN} is controlled by many factors, including formation rate (J), growth rate (GR), background particle number size distribution (PNSD), and properties of the particles. The formation rate is defined as a flux of newly-formed particles at a threshold diameter and is usually used to describe how many particles are produced into the atmosphere during an event. The growth rate (GR) represents the diameter change of the particles in a certain time period, and particles with a higher GR will grow to the CCN sizes in a shorter time. The background PNSD controls the scavenging of the newly-formed particles, and the high concentration of pre-existing particles will efficiently scavenge these particles before they can grow to the CCN sizes. The properties of the particles (e.g., chemical composition, hygroscopicity, and surface tension) affect their ability of acting as CCN. In general, particles containing a higher fraction of inorganic mattermatters or water-soluble organics are more hygroscopic and are more easily activated due to a lower critical diameter (D_{50}). Recent studies showed that surfactant effects of organic matters were found on the particle surface which could lead to an increase of the CCN activity (Ovadnevaite et al., 2017; Cai et al., 2018; Liu et al., 2018). The contribution of NPF to N_{CCN} is difficult to be quantitatively evaluated and currently the major impact factors controlling factors are not fully understood, which becomes a challenging in quantification of the climatic forcing of NPF events.constraining an accurate quantification of the aerosol climatic forcing from NPF.

NPF event iswas well known to have an important contribution to the N_{CCN}, while a wide range of N_{CCN} during NPF events was reported in the literature. Yue et al. (2011) showed that the N_{CCN} during

NPF events was increased by a factor of 0.4-6 in Beijing. However, much less (a factor of 1.17-1.88) increase of the N_{CCN} was observed during NPF events in Shanghai (Leng et al., 2014). The results from Ma et al. (2016) showed that the N_{CCN} was significantly impacted by the hygroscopicity of newly-formed particles during NPF events in the North China Plain (NCP). Yu et al. (2014) reported an average factor of 4.7 increase of the N_{CCN} during NPF events from growth of new particles to the CCN sizes in Ozark forest. Rose et al. (~~2016~~2017) showed that NPF could be a larger contributor to N_{CCN} compared to transport in free troposphere. A long-term field measurement in the urban Vienna conducted by Dameto de España et al. (2017) reported that the N_{CCN} (at 0.5% ss) could increase up to 143% during NPF events. Kalkavouras er al. (2017) found that the NPF could double the N_{CCN} (at 0.1% ss), but could augment the potential droplet number only by 12%.

Factors that control the CCN activity of newly-formed particles (formation rate, growth rate, and particle properties) were investigated worldwide. These parameters varied substantially in a large temporal and spatial scale. For example, the mean formation rate of 10 nm particles (J_{10}) was 3.7 cm^{-3} s^{-1} in Nanjing (An et al., 2015), which was much higher than that (0.40 cm^{-3} s^{-1}) reported in Shanghai (Leng et al., 2014). A value of 3.3~81.4 cm^{-3} s^{-1} was reported for the mean formation rate of 3 nm particles (J_3) based on one-year long measurements in Beijing (Wu et al., 2007). In the NCP region, a long-term measurement conducted by Shen et al. (2011) reported that the J_3 ranged from 0.7 to 72.7 cm^{-3} s^{-1}, with a mean value of 8.0 cm^{-3} s^{-1} . Shen et al. (2019) reported an average J_3 value of 1.30 cm^{-3} s^{-1} at Mountain Tai, which was much lower than urban regions. The growth of newly-formed particles can be characterized by the particle growth rates. Kulmala et al. (2004) summarized a wide range of growth rate (1 to 20 nm h^{-1}) from more than 100 filed measurements of NPF in mid-latitudes. On the one hand, the growth rates are usually high in polluted region, for example, a growth rate of 11.6-18.1

nm h^{-1} was reported in New Delhi, India (Kulmala et al., 2005;Mönkkönen et al., 2005). On the other hand, the growth rates are in general low in forest regions, for example, a median value of 2.5 nm h^{-1} was reported from long term measurements (Nieminen et al., 2014). Furthermore, large uncertainties exist for the measured growth rates even in the same region. For example, the growth rates under sulfur-poor conditions were about 80% higher than those under sulfur-rich conditions in Beijing (Yue et al., 2011). The condensable vapors not only control the growth rate, but also decide the hygroscopicity of newly-formed particle, which can vary in a large range from event to event. Wu et al. (2013a) reported a hygroscopic growth factor of 1.2 to 1.55 during NPF events in a mountain region, Germany. Asmi et al. (2010) found a significant contribution of organic vapors to particle formation and growth, leading to a low hygroscopicity of newly-formed particles in the Antarctica region. The above studies show large temporal and spatial variations of characteristics in the properties of newly-formed particles (i.e., the formation rate, growth rate and hygroscopicity) during NPF events. However, how these parameters contribute to the variation of the N_{CCN} during NPF events in various regions is yet to be investigated.

Although the Pearl River Delta region (PRD), one of the most economically developed areas in China, has made substantial progress in mitigating haze pollution, especially in achieving $PM_{2.5}$ national level II standard (an average annual mass concentration of less than 35 μg m^{-3} for $PM_{2.5}$), the intensive human activities and photochemistry lead to emissions and productions of a large amount of condensable air pollutants for initiating formation of atmospheric particles and promoting their subsequent growth. Several studies have reported the frequent occurrences of NPF events in urban and rural areas of the PRD which provide a large amount of particles to the local atmosphere (Yue et al., 2013;Liu et al., 2008;Yue et al., 2016;Wang et al., 2013). However, these studies focused primarily on

the characteristics of the NPF events, the contribution to the N_{CCN} and the controlling factors were still unknown, hindering an accurate assessment of NPF in CCN formation and eventually global climate change.

In this study, we analyzed the contribution of NPF to the N_{CCN} based on a rural field campaign conducted at the Heshan supersite in the PRD region during Fall (October and November, 2019). A suite of advanced analytical instruments ~~were~~was employed to measure particle hygroscopicity, size-resolved CCN activity, and particle number size distribution (1 nm - 10 μm). Here, we select three representative NPF events (two from this measurement, the other one from a previous measurement in Panyu, Guangzhou, 2014) to quantitively investigate the contribution of NPF to the N_{CCN} and impact factors (i.e., formation rate, growth rate, background particle concentration, and particle properties) that ~~manipulate~~ affect the contribution.

2 Measurement site, instrumentation, and methodology

2.1 Measurement site

The field campaign was conducted at the Heshan supersite in the Guangdong Province of China during the Fall season (from 27th September to 17th November, 2019). This rural site (22°42′39. 1″N, 112°55′35.9″E) is located at the southwest of the PRD region (about 70 km away from megacity Guangzhou) with an altitude of about 40 m above sea-level and the site is surrounded by several farms and villages. All the instruments were placed in an air-conditioned room (T=298K) on the top floor of the building at the supersite, administrated by Guangdong Provincial Environmental Monitoring Centre. Two aerosol sampling ports equipped respectively with a PM_{10} impactor and a $PM_{2.5}$ impactor were

made of a 6 m long 3/8″ o.d. stainless-steel tube. The schematic diagram of the inlet system and instrument setup is shown in Fig. S1. ~~An aerosol sampling port equipped with a PM_{10} cyclone inlet was made of a 6 m long 3/8″ o.d. stainless-steel tube.~~ The sampling air was dried to a relative humidity (RH) lower than 30% by passing through a Nafion dryer (model MD-700, Perma Pure, Inc., USA) before the air entered into the individual instruments.

2.2 Instrumentation

2.2.1 Particle number size distribution and size-resolved CCN activity measurements

The particle number size distribution (PNSD) in a complete size range of 1 nm- 10 μm (an upper cut size of 10 μm) was measured by a diethylene glycol scanning mobility particle sizer (DEG-SMPS, model 3938E77, TSI Inc., USA), a SMPS (model 3938L75, TSI Inc., USA), and an aerodynamic particle sizer (APS, model 3321, TSI Inc., USA). The DEG-SMPS was applied to measure particles with a size range of 1-30 nm, consisted of a nano-differential mobility analyzer (nDMA, model 3086, TSI Inc., USA), a nano enhancer (model 3777, TSI Inc., USA), and a condensation particle counter (CPC, model 3772, TSI Inc., USA). The SMPS composed of a DMA (model 3081A, TSI Inc., USA) and a CPC (model 3775, TSI Inc., USA) was employed to measure particles in a size range of 10-800 nm. The APS was used to measured submicron particles ranging from 0.5 μm to 10 μm. The data inversion processes for the measured PNSD were done by Aerosol Instrument Manager (version 10, TSI Inc., USA). However, accurate inversion for particles smaller than 3 nm is currently still lacking due to large uncertainties from corrections for multiple charges and diffusion losses. Thus, we only discussed PNSD for particles larger than 3 nm in this study.

Size-resolved CCN activity was measured with a combination of a cloud condensation nuclei counter (CCNc, model 200, DMT Inc., USA) and another SMPS. The CCNc-200 has two parallel cloud columns, which can be used to measure the CCN concentration (N_{CCN}) simultaneously. The supersaturation of each column was set to be 0.1%, 0.2% and, 0.4%, 0.7%, 0.9%, and 1.0%, respectively. The dry particles were firstly neutralized by an X-ray neutralizer (model 3088, TSI Inc., USA) and were then classified by a DMA (model 3081A, TSI Inc., USA). The monodisperse particles were split into three streams: two to the CCNc for measurement of the N_{CCN} (with a flow rate of 0.6 LPM) and one to the CPC for measurement of total particle number concentration (N_{CN}, with a flow rate of 0.3 LPM). Prior to the campaign, the SMPSs was calibrated with standard polystyrene latex spheres (PSL, with a size of 20, 50, and 200 nm) and the CCNc-200 was calibrated with ammonium sulfate $((NH_4)_2)SO_4$ particles at the six SSs (0.1%, 0.2%, 0.4%, 0.7%, 0.9%, and 1.0%).

2.2.2 Aerosol hygroscopicity measurement

Hygroscopicity of atmospheric particle at various size ranges was measured by a hygroscopic tandem differential mobility analyzer (HTDMA), consisted of two DMA (model 3081L, TSI Inc., USA), a Nafion humidifier (model MD-700, Perma Pure Inc., USA), a heated tube and a condensation particle counter (model 3788, TSI Inc., USA). The dry particles were firstly neutralizer by an X-ray neutralizer (model 3088, TSI Inc., USA) and subsequently were classified by a DMA for six sizes in this study (30, 50, 80, 100, 150, and 200 nm). The selected particles at a specific diameter (D_0) were then introduced into a humidifier under a fixed RH (90% in this study). Another DMA and a CPC were used to measure size distribution of humified particles (D_{wet}).

2.3 Methodology

2.3.1 Estimation of hygroscopicity based on the measurements

The size-resolved activation ratio (AR) could be obtained from the measured N_{CN} and N_{CCN} by the SMPS and CCNc-200 system and was inverted based on the method described by Moore et al. (2010). The AR was then fitted with the sigmoidal function with respect to particle diameter D_p,

$$\frac{N_{CCN}}{N_{CN}} = \frac{B}{1+(\frac{D_p}{D_{50}})^C} \quad (1)$$

where B, C, and D_{50} are fitting coefficients. The D_{50} represents the critical diameter at which half of the particles are activated at a specific SS.

The hygroscopic parameter κ can be obtained from the critical supersaturation (Sc) and the D_{50} (Petters and Kreidenweis, 2007) by

$$\kappa = \frac{4A^3}{27D_{50}^3(\ln Sc)^2} \text{ , where } A = \frac{4\sigma_{s/a}M_w}{RT\rho_w} \quad (2)$$

where $\sigma_{s/a}$ is the surface tension of the solution/air interface and here it is temporarily assumed to be that of pure water (0.0728 N m^{-1} at 298.15 K), M_w is the molecular weight of water (0.018 kg mol^{-1}), R is the universal gas constant (8.31 J mol^{-1} K^{-1}), T is the thermodynamic temperature in Kelvin (298.15 K), and ρ_w is the density of water (about 997.04 kg m^{-3} at 298.15 K).

The growth factor (GF) of selected particles can be calculated according to the following equation,

$$Gf = \frac{D_{wet}}{D_0} \quad (3)$$

In addition to the hygroscopic parameter calculated based on the SMPS and CCNc-200 system, the κ can also be calculated from HTDMA measurement based on the growth factor,

$$\kappa = (Gf^3 - 1)\left[\frac{1}{RH}\exp\left(\frac{4\sigma_{s/a}M_w}{RT\rho_w D_0} - 1\right)\right] \quad (4)$$

Due to the effect of DMA diffusing transfer function, the TDMAfit algorithm (Stolzenburg and

McMurry, 2008) was applied to narrow the uncertainty and fit the growth factor probability density function (GF-PDF). Detailed data inversion process can be found elsewhere in Tan et al. (2013).

2.3.2 Estimation of H_2SO_4 concentration and its contribution to particle growth

The daytime gas phase H_2SO_4 concentration is estimated according to the proxy proposed by Lu et al. (2019),

$$[H_2SO_4] = 0.0013 \cdot UVB^{0.13} \cdot [SO_2]^{0.40} \cdot CS^{-0.17} \cdot ([O_3]^{0.44} + [NO_x]^{0.41}) \quad (5)$$

where UVB is the ultraviolet radiation B intensity (in W m^{-2}), $[SO_2]$ is the concentration of SO_2 in molecules cm^{-3}, $[O_3]$ is the concentration of O_3 in molecules cm^{-3}, $[NO_x]$ is the concentration of NO_X in molecules cm^{-3}, and the CS is the condensation sink and it can be calculated from following equation,

~~The daytime gas phase H_2SO_4 concentration is estimated according to the proxy presented by Petäjä et al. (2009),~~

~~$$[H_2SO_4] = \frac{k \cdot [SO_2] \cdot [OH]}{CS} \quad (5)$$~~

~~where k is the reaction rate constant and is assumed to be 8.5×10^{-13} cm^3 $molecule^{-1}$ s^{-1} in this study (Chen et al., 2014;Wang et al., 1988;Vignati et al., 2004), $[SO_2]$ is the concentration of SO_2 in molecules cm^{-3}, $[OH]$ is the concentration of OH radical in molecules cm^{-3}, and the CS is the condensation sink in s^{-1} and it can be calculated from following equation,~~

$$CS = 2\pi D \sum_{Dp_i = Dp_{min}}^{+\infty} \beta_m N_i \quad (6)$$

where D is the diffusion coefficient of the H_2SO_4 vapor (assumed to be 0.8×10^{-5} m^2 s^{-1} in this study), $\beta_{m,i}$ is the transitional regime correction factor which can be calculated from the Knudsen number (Fuchs and Sutugin, 1971), and N_i represents the particle number concentration at Dp_i.

This proxy is derived based on measurements from a winter field measurement in urban Beijing, where the atmospheric environment is similar to the locations of our measurements. A relative error of about 20% for the proxy proposed by Lu et al. (2019) was estimated based on comparison of the estimated [H_2SO_4] with the measured one. However, accurate quantification of the uncertainty is not feasible since this proxy has not been tested in the PRD region. For simplicity, we adopted a relative error of about 20% for the estimation of sulfuric acid concentration, and ignoring the uncertainties in measuring UVB, [SO_2], CS, [O_3] and [NO_X]. However, further investigation is still needed, since the relative error of the estimation could vary temporally and spatially (Mikkonen et al., 2011). –

Framework for 0-D Atmospheric Modeling (F0AM) v3.1(Wolfe et al., 2016) is a zero-dimensional atmospheric box model which was used to simulate the concentration of OH radical in the atmosphere. The model was constrained with a set of online measured trace gases, VOCs, and meteorological data. The employed chemical mechanism is Master Chemical Mechanism (MCM) v3.3.1. More detailed description of model setup can be found in Wang et al. (2020).

The required vapor concentration of H_2SO_4 ($C_{v,GR=1\ nm\ h^{-1}}$) for a growth rate of 1 nm h^{-1} in a certain particle size range ($D_{p,initial}$ to $D_{p,final}$) can be calculated from the following equation,

$$C_{v,GR=1\ nm\ h^{-1}} = \frac{2\rho_v d_v}{\alpha_m m_v \Delta t} \cdot \sqrt{\frac{\pi m_v}{8kT}} \cdot \left[\frac{2x_1+1}{x_1(x_1+1)} - \frac{2x_0+1}{x_0(x_0+1)} + 2ln\left(\frac{x_1(x_0+1)}{x_0(x_1+1)}\right)\right] \quad (8)$$

where ρ_v, m_v and D_v is the density, mass and diameter of H_2SO_4, which was assumed to be 1830 kg m^{-3}, 98 amu, and 0.55 nm, respectively (Nieminen et al., 2010;Jiang et al., 2011), α_m is the mass accommodation coefficient (assumed to be unity in this study), x_1 and x_0 are the ratios of D_v to $D_{p,final}$ (10 nm in this study) and $D_{p,initial}$ (3 nm in this study), Δt (in s) is the time for particle growth from $d_{p,initial}$ to $d_{p,final}$ ($\Delta t = \frac{d_{p,final} - d_{p,initial}}{GR}$) with a growth rate of 1 nm h^{-1}, and k is the Boltzmann constant (1.38×10^{23} J K^{-1}).

Thus, the growth rate contributed from condensation of H_2SO_4 vapor can be obtained,

$$GR_{H_2SO_4} = \frac{[H_2SO_4]}{C_{v,GR=1\ nm\ h^{-1}}} \quad (9)$$

The average calculated H_2SO_4 concentration during particle growth can be calculated using Eq. (5). The resultant $GR_{H_2SO_4}$ can be overestimated because the assumption of unity for α_m in Eq. (8) is not necessarily the case because not all H_2SO_4 molecules will be captured when colliding with the particles.~~not necessary the case because not all H_2SO_4 molecules end up loss for their collisions with pre-existing particles.~~

2.3.3 Estimation of growth rate (GR) and formation rate (J)

The observed particle growth rate (GR) is defined as the diameter change of nucleated particles (dDp_{nuc}) for a time period (dt),

$$GR = \frac{dDp_{nuc}}{dt} \quad (10)$$

Here log-normal distribution function method was adopted and the PNSD was fitted to obtain the representative diameter for nucleated particles during NPF events (Kulmala et al., 2012),

$$\frac{dN}{dlogD_p} = \frac{N}{\sqrt{2\pi}\sigma} exp\left(-\frac{ln^2(\frac{Dp}{Dp_{gmd}})}{2\sigma}\right) \quad (11)$$

where D_p is particle diameter, N is total particle number concentration, Dp_{gmd} is geometric mean particle diameter and it was also used as the representative particle size in Eq. (10). In this study, the PNSD was found to have a significant mode in a size range of 3- 60 nm during NPF events and we hence applied one log-normal mode fitting. At each time step, the PNSD was fitted using Eq. (11) and the Dp_{gmd} as a function of time, that is, the growth rate, was determined according to Eq. (10).

The formation rate (J_k) described the flux through a certain diameter (k) during NPF events and it

is calculated based on the formula given in Cai and Jiang (2017),

$$J_k = \frac{dN_{[Dp_k,Dp_u)}}{dt} + \sum_{Dp_g = Dp_k}^{Dp_{u-1}} \sum_{Dp_i = Dp_{min}}^{+\infty} \beta_{(i,g)} N_{[Dp_i,Dp_{i+1})} N_{[Dp_g,Dp_{g+1})} -$$

$$\frac{1}{2} \sum_{Dp_g = Dp_{min}}^{Dp_{u-1}} \sum_{Dp_i^3 = \max\left(Dp_{min}^3, Dp_k^3 - Dp_{min}^3\right)}^{Dp_{i+1}^3 + Dp_g^3 \le Dp_u^3} \beta_{(i,g)} N_{[Dp_i,Dp_{i+1})} N_{[Dp_g,Dp_{g+1})} + n_u \cdot GR_u \quad (12)$$

where $N_{[Dp_k,Dp_u)}$ is particle number concentration in a size range from Dp_k to Dp_u (exclude particles with diameter Dp_u), Dp_k and Dp_u are the lower and upper bound diameters (here 3 and 30 nm respectively), $\beta_{(i,g)}$ is the coagulation coefficient for collisions between particles with diameter Dp_i and particles with diameter Dp_g, n_u is the particle distribution function at Dp_u and GR_u is the growth rate calculated using Eq. (10) at Dp_u. Note that the calculation of formation rate using Ep. (12) is based on two assumptions: (1) Dilution and other particles sources and losses except for coagulation loss in the size range from Dp_k to Dp_u are negligible; (2) Net coagulation of particles is negligible.

2.3.4 Measurement based NPF simulations

For a regional NPF event, the evolution of particle size distribution is governed by the population balance equations (Lehtinen et al., 2003; Kuang et al., 2012):

$$\frac{dN_{k^*}}{dt} = J_{k^*} - GR \cdot n_{k^*} - N_{k^*} \sum_{Dp_i = Dp_{min}}^{+\infty} \beta_{(k^*,i)} N_i$$

(13-1)

$$\frac{dN_k}{dt} = GR \cdot n_{k-1} - GR \cdot n_k + \frac{1}{2} \sum_{Dp_i = Dp_{min}}^{k-1} \beta_{(i,\varphi)} N_i N_\varphi - N_k \sum_{Dp_i = Dp_{min}}^{+\infty} \beta_{(k,i)} N_i \quad (13\text{-}2)$$

$$Dp_\varphi^3 = Dp_k^3 - Dp_i^3$$

(13-3)

In the equations, class k^* represents the smallest detectable ~~stable~~ particle (here 3 nm particles), J_{k^*} is the formation rate calculated using Eq. (12). Class k represents the particles with diameter Dp_k. The first, second, and third terms on the right-hand side (RHS) of Eq. (13-1) represent the formation,

condensation, the coagulation sink terms, respectively. The first and second terms, the third, and fourth terms on the RHS of Eq. (13-2) represent the condensation growth terms, a coagulation source (CoagSrc) term, and the coagulation sink (CoagSnk) term, respectively.

For a specific NPF event, the evolution of PNSD with a size range of 3-1000 nm was simulated based on Eq. (13) using Matlab (version 2016a, Mathworks, Inc.). In the simulation, the background particle distribution was assumed to be the average PNSD before 6:00 LT, the growth rate and formation rate were the measured values obtained from Eq. (10) and Eq. (13), respectively, and the time step was set to be 10s. The simulation is based on following assumptions: (1) The dynamics of newly-formed particles are driven by coagulation and condensation. The influences of transportation, primary emissions, dilution, and particle evaporation are negligible. (2) The influence of coagulation on the preexisting particles is negligible. (3) The particle growth rate for all particle sizes is assumed to be the same at a time during NPF events.

3 Results and discussion

3.1 New Particle Formation (NPF) events at the Heshan Site

A total of 20 NPF events were observed during this seven-weeks long field campaign. Here we selected a typical event (29th October, 2019) for further investigation. As shown in Fig. 1a, new particle formation occurred at about 9:50 Local Time (LT) when a significant concentration of 3-10 nm particles were observed. Subsequently, continuous and steady growth of the newly-formed particles was observed until the particles grew to about 70-80 nm at about 20:00 LT. The blue dots in Fig.1a represent the Dp_{gmd} of nucleated particles and the red line represents the linear fitting, leading to an

estimated growth rate of 8.0 nm h^{-1}. Prior to the event (around 9:50), the total particle number concentration (N_{CN}) remained low (a concentration slightly below 10000 cm^{-3}) and rapidly increased when NPF event occurred, and then reached its peak (about 56000 cm^{-3}) at 11:15 LT and subsequently decreased to 20000 cm^{-3} at about 15:00 LT, and remained at this concentration for the rest of the day. A steady north wind was observed before 18:00 LT and shifted to northwest afterwards (Fig. 1c). The shift of wind direction led to change of air mass as seen from the PNSD, leading to a sudden increase of the N_{CN} at 18:00 LT (Fig. 1a and b). The CCN concentration (N_{CCN}) at 1.0% SS increased from 5000 cm^{-3} at around 10:00 to 11000 cm^{-3} at about 15:00 LT, when the nucleated particles grew to the CCN size (Fig. ~~S1~~S2). The D_{50} at 1.0% SS was apparently the smallest critical diameters among all the SSs, the size that was easily reached during NPF and was significantly affected by the newly-formed particles, we thus only discussed the variation of the N_{CCN} at 1.0% SS in the following section. The sudden increase of N_{CCN} at 18:00 LT could be attributed to change of the air mass due to transportation, consistent with the changes of the PNSD, the N_{CN}, and wind direction (Fig. 1a-c). The activation ratio (AR) was about 0.5 before dawn and dropped to about 0.2 just prior to the event (Fig. 1b). This ratio continued to decrease to its trough at the time corresponding to the maximum of N_{CN} and then increased again to about 0.6 at 15:00 LT during particle growth, slightly higher than the value before dawn. Clearly, NPF can not only add a large number of particles to the atmosphere but also increase the N_{CCN} and AR after particles are formed and grow. The wind speeds were about 3 m s^{-1} during initial formation and growth, and decreased to about 1.5 m s^{-1} during most of the particle growth periods.

Formation of gaseous H_2SO_4 was favored by intensive photochemistry. Significant j-values of $O(^1D)$ (in s^{-1}) were observed during the day (from about 7:00 to 17:00) with a maximum value of 2×10^{-5} s^{-1} at noon and symmetrically distributed before and after noon. The average calculated H_2SO_4

concentration during particle formation periods (10:00-12:00 LT) was about 1.4×10^7 cm^{-3}, about an order higher than that (about 7 - 12×10^6 cm^{-3}) in a mountain region in Germany (Wu et al., 2013) and close to that (about 2-5 $\times$ 10^7 cm^{-3}) in a rural region of Sichuan in China (Chen et al., 2014). Considering a relative error of about 20%, the growth rate contributed by condensation of gaseous H_2SO_4 was about 0.61-1.09 nm h^{-1}, or about 7.6% -13.6% of the observed growth rates for 3-10 nm particles. It should be pointed out that the above estimates for the growth rates are subject to large uncertainties due to uncertainties for the estimation of sulfuric acid concentration using Eq. (5) as the proxy and here a unity of sticking coefficients was assumed when gaseous H_2SO_4 molecules collide with pre-existing particles. ~~The average calculated concentration of H_2SO_4 during particle formation (10:00-12:00 LT) was about 1.9×10^7 cm^{-3}, about an order higher than that (about 7 - 12×10^6 cm^{-3}) in a mountain region in Germany (Wu et al., 2013a) and close to that (about 2-5$\times10^7$ cm^{-3}) in a rural region of Sichuan in China (Chen et al., 2014). Considering an uncertainty of 40% in estimation of H_2SO_4 concentration (Wu et al., 2013b), the GR contributed by condensation of gaseous H_2SO_4 only was about 0.78-1.12 nm h^{-1}, or about 5.6% -20.0% of the total observed particle growth rate in a size range of 3-10 nm.~~ This implies that other compounds (e.g., organic vapors) than H_2SO_4 play significant roles in the growth process of newly-formed particles which was widely reported in literatures (Boy et al., 2005;Casquero-Vera et al., 2020;Paasonen et al., 2010).

3.2 The impact of hygroscopicity and surfactants on N_{CCN}

The ability that atmospheric particles can serve as CCN is determined by several factors including sizes, chemical composition, surface tension, and water saturation ratio of the particles (Farmer et al., 2015). The organic matter in particles can act as surfactants to lower the surface tension of the particles

and hence can increase the CCN activity (Ovadnevaite et al., 2017). Previous studies showed that surfactants could modify the ability of water uptake, leading to discrepancies of κ values between measurements using techniques under different water saturation conditions, e.g., sub-saturation (HTDMA measurements) or supersaturation (CCNc measurements) (Cai et al., 2018; Wex et al., 2009; Rastak et al., 2017; Ruehl and Wilson, 2014).~~Previous studies showed that the presence of surfactants led to discrepancies of κ values between measurements using different techniques under sub-saturation (HTDMA measurements) or supersaturation conditions (CCNc measurements) (Cai et al., 2018; Wex et al., 2009; Rastak et al., 2017).~~ Figure 2 compares the κ values measured from several locations including Heshan (this study, rural), Panyu (urban PRD, Cai et al., 2018, 2019), and South China Sea (Cai et al., 2020). The median κ values measured by HTDMA in this study ranged from 0.1 to 0.18 in a size range of 30-200 nm, similar to those of particles primarily composed of organics (Deng et al., 2018;Liu et al., 2018;Pajunoja et al., 2015), implying that chemical composition of the measured particles was dominated by organics. In particular, the κ values measured using HTDMA (κ_{HTDMA}) in this study were significantly lower than those from other studies. The κ values in a range of 0.21-0.31 were reported for urban PRD and suburban North China Plain, which were likely attributed to high fractions of water-soluble organic matters and inorganic compounds from traffic and industry emissions. The κ values measured using CCNc (κ_{CCN}) fall in a range from 0.19 to 0.46, much higher than those from measurements using HTDMA in this study. The discrepancy of the κ κ_{HTDMA} and κ_{CCN} values suggests that surfactant effects could play an important role in CCN activation under sub-saturation and supersaturation environments. Previous studies have shown that the organics in particles could lower surface tension by about 0.01-0.032 N m^{-1} (Ovadnevaite et al., 2017; Liu et al., 2018; Engelhart et al., 2008; Cai et al., 2018), leading to the decrease of the D_{50} and higher κ values. This effect was closely

related to the presence of liquid-liquid phase separation (LLPS) (Renbaum-Wolff et al., 2016), which was observed in organic-containing particles under high relative humidity. LLPS is mainly depended on the chemical composition of organics (e.g., functional groups and oxidation state) and inorganic-organic mixing ratio (Ruehl et al., 2016; Ma et al., 2021; Bertram et al., 2011). Once LLPS occurred, organic-rich phase on the droplet surface would reduce surface tension and further enhance water uptake (Rastak et al., 2017;Freedman, 2017). Surface tension is expected to increase with droplet growth, since the organic-rich phase becomes thinner and shifted to water-rich phase (Liu et al., 2018; Renbaum-Wolff et al., 2016; Ovadnevaite et al., 2017). Further laboratory and field studies are needed for better understanding the occurrence of LLPS in particles, its variation with different chemical composition, and its impact on the surface tension.

A surface tension value ($\sigma_{s/a}^{*}$=0.060 N m^{-1}) was adopted to calculate both the κ_{CCN} (denoted as $\kappa_{CCN\ \sigma_{s/a}^{*}}$) and κ_{HTDMA} ($\kappa_{HTDMA\ \sigma_{s/a}^{*}}$) using Eq. (2) and Eq. (4), respectively. No significant changes of κ values (i.e., from 0.11 to 0.10 for 30 nm particles) were found from TDMA measurements (Fig. S3), while the κ values from CCNc measurements using this surface tension value ($\sigma_{s/a}^{*}$) were still lower than those using pure water assumption and the differences became larger with increasing particle sizes, implying that the surface tension is dependent on particle diameter. It also implies that the κ value was more susceptible to surfactants under supersaturation condition, which can lower the D_{50} of the particle for facilitating CCN activation.~~A new surface tension ($\sigma_{s/a}^{*}$=0.060 N m^{-1}) was adopted to calculate the κ_{CCN} using Eq. (2) based on the measured critical diameter (D_{50}), which brought the κ_{CCN} values at SS=1.0% and 0.9% within those of κ_{HTDMA}, although the κ_{CCN} values with this new $\sigma_{s/a}^{*}$ at other SSs were still higher, implying that the surface tension is dependent on particle diameter. Surfactants can lower the D_{50} of the particle which then facilitates its activation as CCN.~~ For particles with the same κ

value, the measured D_{50} (denoted as $D_{50,m}$) by fitting of N_{CCN}/N_{CN} using Eq. (1) was lower than the calculated value based on pure water surface tension using Eq. (2) due to the surfactant effect. In order to estimate the impact of surfactant on particle activation, the D_{50} was recalculated using the surface tension of pure water (0.072 N m^{-1}) by Eq. (2) based on the κ value from the CCN measurements with a surface tension correction (refer to κ_{CCN} $\sigma_{s/a}^*$ and $\sigma_{s/a}^*$=0.060 N m^{-1} in Fig. 2). We termed the above recalculated D_{50} as the $D_{50,r}$ ~~D_{50} $\sigma_{s/a}$~~ to illustrate the surfactant effects on the CCN activity during NPF events. Figure 3 shows the variation of the $D_{50,r}$ ~~recalculated D_{50}~~ (here $\sigma_{s/a}$=0.072 N m^{-1}) and the $D_{50,m}$ ~~measured D_{50}~~, along with the Dp_{gmd} of the nucleated particles during the NPF event. The $D_{50,m}$ ~~measured D_{50}~~ was lower than the $D_{50,r}$ ~~recalculated D_{50}~~ by about 10 nm. As a result, the Dp_{gmd} reached the $D_{50,m}$ ~~measured D_{50}~~ at about 15:00 LT, about two hours earlier than it arrived at the $D_{50,r}$ ~~recalculated D_{50}~~, which indicates that the surfactant effects could lead to earlier activation of the newly-formed particles as CCN. The earlier the Dp_{gmd} reaches the critical diameter D_{50}, the higher the N_{CCN} is because more particles can survive from being scavenged by preexisting particles. The difference of PNSD at the time when the Dp_{gmd} reached respectively the $D_{50,m}$ ~~measured D_{50}~~ and the $D_{50,r}$ is shown in Fig. S2 ~~recalculated D_{50} was shown in Fig. 1S~~. The peak value of PNSD at 15:00 LT was about 20000 cm^{-3} higher than the value at 17:15 LT. The N_{CCN} also shows a difference between the $D_{50,r}$ and $D_{50,m}$ (Fig. 4a).

We also investigate the effect of the surface tension on the N_{CCN} at SS=1.0% by varying the value of the surface tension. As we mentioned in the beginning of this section, a surface tension of 0.060 N m^{-1} ($\sigma_{s/a}^*$) was adopted when discussing the CCN activation at 1.0% SS and we assume that the $D_{50,r}$ ~~recalculated D_{50}~~ was based on this surface tension value. The average D_{50} (denoted as $D_{50,a}$) was the mean of the $D_{50,m}$ ~~measured and recalculated D_{50}~~. The N_{CCN} is calculated by integrating particle

concentrations above D_{50} using the following equation,

$$N_{CCN} = \int_{D_{50}}^{\infty} n_i dlogDp_i \quad (14)$$

where n_i is the particle distribution function at Dp_i. The D_{50} can be the measured or recalculated one. It was shown that the N_{CCN} at SS=1.0% from integration of particles above the $D_{50,r}$ ~~recalculated D_{50}~~ was significantly lower than that above the $D_{50,m}$ ~~measured D_{50}~~ after 12:00 LT (two hours after the occurrence of the NPF event), with concentration differences of about 3000-4000 cm^{-3} (Fig. 4a). The AR based on the $D_{50,r}$ ~~recalculated D_{50}~~ reached its minimal values between 10:00 and 12:00 LT, and then steadily increased until 22:00 and subsequently decreased. The AR based on the $D_{50,m}$ ~~measured D_{50}~~ reached its minimal during the same period as the AR from the $D_{50,r}$ ~~recalculated D_{50}~~; however, it then rapidly increased until 16:00 and the continuing increase of the AR was much slower until 22:00, and also subsequently decrease for the last hour of the measurement (Fig. 4b). This different trend was likely attributed to the continuing growth of the nucleated particles to the CCN size prior to 16:00. Here, we define the deviation of N_{CCN} based on the $D_{50,r}$ ~~recalculated D_{50}~~ from that based on the $D_{50,m}$ ~~measured D_{50}~~ to evaluate the impacts of the surface tension (primarily due to the surfactant effects) on the N_{CCN},

$$\delta_{N_{CCN}} \equiv \frac{N_{CCN,m} - N_{CCN,r(or\ a)}}{N_{CCN,m}} \quad \sout{\delta_{N_{CCN}} = \frac{N_{CCN,m} - N_{CCN,r}}{N_{CCN,m}}} \quad (15)$$

where the $N_{CCN,m}, N_{CCN,r}$ represent the N_{CCN} based on the $D_{50,m}$ ~~measured D_{50}~~ and the $D_{50,r}$ ~~recalculated D_{50}~~ or $D_{50,a}$ ~~average D_{50}~~. The $\delta_{N_{CCN}}$ of the $D_{50,r}$ ~~recalculated D_{50}~~ was about 0.1 prior to the NPF event, and reached a peak value of 0.4 at 14:00 LT, and then decreased steadily to 0.1 at 22:00 and remained unchanged for the last hour of the measurement (Fig. 4c). The results suggests that the decrease of the surface tension due to the surfactant effects could lead to about 10% increase of the N_{CCN} at 1.0% SS

for non-event period and about 40% increase during the NPF event (Fig. 4c). Apparently, the surfactants have more significant effects on N_{CCN} during the NPF event period than during non-event period, as the difference between the $\delta_{N_{CCN}}$ based on the $D_{50,r}$ ~~recalculated D_{50}~~ and the $D_{50,a}$ ~~average D_{50}~~ was significant only during the event period (12:00-18:00 LT).

The hygroscopicity of newly-grown particles can have significant impact on the N_{CCN} during the NPF event. During the campaign, the minimum particle size of CCN activity measurement was about 40-45 nm (at 1.0% SS), thus the hygroscopicity of this size range was used to present the property of the newly-grown particles, when they grow up to this size range. In general, the κ_{CCN} values for 40-45 nm particles were significantly higher (corresponding to much higher hygroscopicity) during early event period than during non-event and other event periods (Fig. S4a). Hence, we adopted a minimum size range of 40-45 nm particles for CCN activity measurements (at about 1.0% SS) to represent typically growth of newly-formed particles to this size range during the campaign. It should be pointed out that the high κ values during 10:00~12:00 LT did not represent the hygroscopicity of the newly-grown particles which were primarily composed of particles much smaller than 30-40 nm. Those new particles grew to about 40-50 nm at 14:00-16:00 (Fig. 1a and Fig. 3) and their κ values were obviously lower than the average ones, implying that the organic vapors could play an important role during growth of new particles as discussed in Section 3.1. ~~The hygroscopicity of newly-formed particles can have profound impact on the N_{CCN} during the NPF event. During the campaign, the minimum particle size of CCN activity measurement was about 40-45 nm, thus the hygroscopicity of this size range was used to present the property of newly-formed particles. In general, the hygroscopic parameter κ values for particles with a size range of 40-45 nm were significantly higher during the early event period than during the non-event and other event periods, corresponding to much higher~~

~~hygroscopicity during the early event period than during the non-event and other event periods (Fig. S2a). The calculated H_2SO_4 concentration peaked at about 10:00-11:00 and subsequently decreased to a low level (about 0.5×10^7 cm^{-3}) until 16:00, implying that the increase of hygroscopicity was related to the condensation of H_2SO_4 vapors. It should be pointed out that the high κ values during 10:00-12:00 LT did not represent the hygroscopicity of newly-formed particles which were primarily composed of particles much smaller than 30-40 nm. Those newly-formed particles grew to about 40-50 nm at 14:00-16:00 (Fig.1a and Fig.3) and their κ values were obviously lower than the average ones, implying that the organic vapors could play an important role during growth of newly-formed particle as discussed in Section 3.1.~~ The decrease of hygroscopicity due to condensation of organic vapors can lead to an increase of about 3-4 nm for the D_{50}, much smaller than the increase of about 10 nm induced by the surfactant effect which reduces the surface tension as discussed before. The results indicate that the surfactant effect may play a more important role than hygroscopicity in the N_{CCN} because the surfactant effect can largely decrease the D_{50} during the NPF event when the number concentration of particles is dominant by Aitken mode.

3.3 The impact of the dynamic processes on N_{CCN}

As discussed in section 2.3.4, the dynamical processes for new particles during nucleation events are governed by the population balance equation (Eq. (13)).~~As discussed in section 2.3.4, the dynamical processes for newly-formed particles during nucleation events are governed by the population balance equation (Eq. (13)).~~ Here, we build a MATLAB program to model the NPF event using Eq. 13, with input parameters including background particle distribution, growth rate and formation rate. Notice that the simulation is based on the aforementioned three assumptions. Figure 5

shows the measured and modeled PNSD, N_{CN}, and N_{CCN} at 1.0% SS. To be simplified, the background particle distribution was assumed to be the average particle distribution before 6:00 LT. The modeled PNSD and N_{CN} agree very well with the measured ones, except the model fail~~fell~~ to reproduce the abrupt change of PNSD and N_{CN} between 18:00 and 22:00. As discussed in section 3.1, this discrepancy was attributed to the change of the air mass by wind direction which was not considered in the model. However, there are considerable discrepancies between the modeled and the measured N_{CCN}. The measured N_{CCN} at 1.0% SS increased steadily after the occurrence of the NPF event (at around 9:00 LT) due to formation of high concentration particles at a size range of 10-60 nm until around 19:00 and subsequently the N_{CCN} dropped for the rest of the day. The model N_{CCN} started to increase at about 14:15 LT and reached its maximum level at about 17:00 LT. The model failed~~fell~~ to reproduce the increase of the measured N_{CCN} before 16:00, although the reasons corresponding to the discrepancy are still unknown. The modeled peak value of the N_{CCN} at 1.0% SS was about 12000 cm^{-3}, which agreed very well with the measured one (11000 cm^{-3}). Again, the model failed~~fell~~ to reproduce the increase of N_{CCN} due to the change of the air mass between 18:00 and 22:00.

As discussed in section 3.2, the contribution of N_{CCN} was affected by the properties of newly-grown particles. However, the characteristics of NPF, including growth rate, formation rate and the background PNSD also affect N_{CCN}. The effects of variation (halving or doubling) of the growth rate, formation rate, and the background PNSD on the N_{CN} and N_{CCN} were investigated to test the sensitivity of those parameters. Figure 6 shows the comparison of the measured N_{CN} and N_{CCN} with their respective modeled values~~the comparison of the measured N_{CN} and N_{CCN} and the modeled one~~ based on the half or doubling of each tested parameter, respectively. As can be seen from Fig. 6a, the modeled N_{CN} values based on the double GR, the double formation rate and the half background PNSD

were higher than the corresponding measured values, respectively, and vice versa. Doubling of the formation rate lead to formation of more new particles and the half background PNSD corresponds to a low coagulation loss with pre-existing particles, resulting in production of more new particles in the simulation. Doubling of the GR resulted in a higher concentration of particles, probably due to the significant increases of the coagulation source (Fig. ~~S3b~~S5b), while small decreases for both of the coagulation sink and growth term were found (Fig. ~~S3a~~ S5a and Fig. ~~S3d~~S5d). Coagulation source means that two smaller particles collide with each other and become a larger particle, which can also increase the population of new particles. Since the newly-formed particles can grow to larger sizes under a higher GR, the PNSD of new particles would be broader (Fig. S~~4~~6), which provides a wider "region" for the coagulation sources, i.e. the "$k-1$" in eq. (13-2) is higher. Doubling of the FR (J) resulted in the highest modeled N_{CN} (about 90000 cm^{-3}) among all simulated cases; however, the modeled N_{CCN} based on a double J was only the second highest value (about 15000 cm^{-3}). The highest modeled N_{CCN} (about 25000 cm^{-3}) was found to double the GR and moreover it peaked earlier at about 14:00 LT (two hours earlier than the other cases). Similarly, the highest modeled AR (about 0.82) was from doubling the GR and an earlier peak time was also found (Fig. ~~S5~~S7). The above results can be attributed to the following two possible reasons: (1) Doubling of the GR made newly-formed particles grow faster to the D_{50} which facilitated the survival of more particles from coagulation scavenging; (2) The N_{CN} became higher by doubling the GR. If newly-formed particle grew slowly, for example, the decrease of the GR to a half value would result in growth of most particles to diameters below that of the D_{50}, leading to the smallest change of the N_{CCN} compared to other cases (Fig. ~~S5~~S7). The pre-existing background particles can serve as the coagulation sinks for newly-formed particles and hence can prevent them from growing to the CCN sizes. For example, under the double background

PNSD condition, the N_{CN} reached its peak of about 38000 cm^{-3} at about 11:00 and quickly dropped afterward. The newly-formed particles contributed about 3000 cm^{-3} to the N_{CCN}, or an AR of about 0.45 at about 17:30 LT, an insignificant change compared to the value for the non-event period, implying that under a high background particle concentration, NPF events have a minor contribution to the N_{CCN}. Doubling or halving of the FR resulted respectively in contribution of about 11000 and 5000 cm^{-3} to the N_{CCN}; however, the magnitude of contribution from variation of the FR was relatively lower than that from the GR and the background PNSD.

Figure 7 shows the comparison of the itemized absolute and fractional contribution of coagulation sink, coagulation source, GR and J to the N_{CCN} for the above several scenarios (model, double GR, half or double J, and half or double PNSD). Here, the individual contribution was integrated from the corresponding term in Eq. (13) for all particle sizes from the initial time of the NPF event to the time when the N_{CCN} reached the peak concentration. As clearly shown in Fig. 7, the coagulation source term plays an more important role in the N_{CCN} (with a fraction of about 13%) for the double GR case than any other cases. As discussed above, doubling of FR (J) and halving of PNSD led to similar N_{CCN} peak values (about 15000 and 13500 cm^{-3}, respectively); however, the dynamics processes for the two scenarios were significantly different. For the double J case, the formation term contributed about 240000 cm^{-3} to the N_{CCN}, much higher than the half PNSD case, and the CoagSnk and CoagSrc terms were much higher (about -260000 and 50000 cm^{-3}, respectively) than any other cases due to formation of high concentration of newly-formed particles. Moreover, under the double J scenario, the fraction of CoagSnk term was higher, while the CoagSrc term was lower than the half PNSD case, indicating a more significant coagulation scavenging with preexisting particles. As a result, the N_{CN} quickly dropped from its peak value to a concentration level similar to the half PNSD case within one hour (Fig.

6a). Based on the above reasons, the contribution of the newly-formed particles to the N_{CCN} was relatively smaller for the double J case than the double GR or half PNSD cases, although its coagulation source term and J term were the highest among all the cases.

To compare different impacts of the characteristics and properties of newly-formed particles, the N_{CCN} was simulated through varying parameters of different characteristics (case 1, 4 and 7) and properties (case 2, 3, 5, 6, 8 and 9). The input parameters for different cases are shown in Table S1. For case 2, 3, 5, 6, 8 and 9 scenarios, the surface tension or hygroscopicity was adjusted to match similar N_{CCN} values based on different NPF characteristics (case 1, 4 and 7, respectively). The results show that doubling GR produces the most significant impact on the N_{CCN}, and the surface tension (κ value) was adjusted to 0.030 N m^{-1}(1.2) to have the same impact (Fig. 8a). Obviously, a κ value of 1.2 for hygroscopicity is much higher than that of many inorganics, e.g., H_2SO_4 (κ=0.90, Topping et al., 2005) and NH_4NO_3 (0.58, Topping et al., 2005). Meanwhile, the surface tension was lower than the values (0.049-0.060) reported previously (Ovadnevaite et al., 2017; Engelhart et al., 2008; Cai et al., 2018). However, doubling GR value (16.0 nm h^{-1}) was reasonable and consistent with previous studies (Mönkkönen et al., 2005; Foucart et al., 2018; O'Dowd et al., 1999), suggesting significant contribution of GR to the growth. For doubling formation rate and halving PNSD, the modified surface tension and κ values were minor (Fig. 8b and c).

3.4 Modeling of the impact factors on the N_{CCN} during NPF events

Here we include two more NPF events to investigate the influence of several important impact factors (growth rate, formation rate, and background particles) on the N_{CCN}, one from this campaign (October 18th, 2019), another from the field campaign in Panyu (December 12th, 2014). Both

campaigns were conducted in the PRD region, details of the field campaign in Panyu can be found in Cai et al. (2018). We applied the same model to simulate NPF as discussed in the previous section. Figure 8 shows the measured (a), modeled (b) PNSD, along with the N_{CN} (c). For a better comparison among all the cases, all the modeled PNSDs were based on the measured formation rate (J_{10}) due to lack of measurement data for particles below 10 nm in the Panyu campaign. The background particle distributions were assumed to be the average values before 7:00 LT. In addition, since no measurement data were available for the CCN activity at 1.0% SS during the Panyu campaign, the N_{CCN} for this campaign was calculated from the average CCN activation curve at 1.0% SS in the two Heshan events and the PNSD of the Panyu event using following equation,

$$N_{CCN} = \int_{Dp_i = Dp_{min}}^{\infty} AR_i n_i dlogDp_i \quad (16)$$

where the AR_i is the average activation ratio (in Heshan) at Dp_i and the n_i is the particle distribution function (in Panyu) at Dp_i.

In general, the modeled PNSDs agreed well with the measured ones for the NPF events under investigation (Fig. ~~8~~9a-f). The N_{CN} values were excellently predicted during the initial particle formation period before the maximum values were reached (Fig. ~~8~~9g-i). In particular, the N_{CN} was well predicted for the study case (the October 29 event) except for the period when the air mass changed as has been discussed in the previous section. For the October 18 event, however, the model underpredicted the N_{CN} shortly after it reached the peak value which can be attributed to significant variation of Aitken mode during the event. For example, the model failed to reproduce concentration trend of 10-60 nm particle at the early event stage (Fig. 10a-b). For the December 12 event, the model underpredicted a significantly lower peak concentration (about 4100 cm^{-3} lower) at about 12:00 pm than the measured one, due probably to presence of a significant amount of larger background particles

(100-200 nm) which were not taken into account in the model (Fig. 9c and Fig. 10c). As a result, the N_{CCN} was underpredicted in two Heshan events (fig. 10a- b), owing to the fluctuation of background particle distribution and unexplained increase of concentration of particles at a size range of 10-60 nm at the beginning of event. ~~For the October 18 event, however, the model began to underpredict the N_{CN} shortly after the N_{CN} reached the peak value, while~~ While for the Panyu event (the December 12 event), a significant underestimate (about 4100 cm^{-3} lower than the measured N_{CN}) for the peak concentration was made at about 12:00 pm, due probably to the presence of a significant amount of other bigger background particles (100-200 nm) after 12:00 pm which was not able to be taken into account in the model (Fig. ~~8~~9c). ~~As a result~~Thus, the predicted N_{CCN} value was substantially lower than the measured one for the December 12 event (Fig. 9c). This also indicates that the N_{CCN} was primarily contributed from the background preexisting particles rather than newly-formed particles form the NPF event in the December 12 event case. The maximum modeled peak N_{CCN} value (about 7000 cm^{-3}) is significantly lower that of the other two events (about 15000 and 12000 cm^{-3}, respectively), which could be attributed to the lower growth rates, formation rate, and the high CS value (Fig. S6 for J_{10} and table S1 for GR and CS). We further simulate the December 12 event to investigate the most important impact factor that influences the N_{CCN} using different characteristics from the two other NPF events (Fig. 11), including the growth rate on the October 18 event (high growth rate scenario), the formation rate on the October 29 event (high formation rate scenario) and the background PNSD on the October 29 event (mainly distributed in Aitken mode, denoted as low CS PNSD scenario). The results show that all the new modeled N_{CN} value were higher than the initial modeled N_{CN} value. The N_{CN} was significantly increased and earlier peaked (with a peak value about 38000 cm^{-3}) under the high formation rate scenario, while the N_{CCN} was mainly affected and also earlier peaked under the high growth rate

scenario. The peak value of N_{CCN} increased from 6000 cm^{-3} to 14000 cm^{-3} and the peak time varied from 20:00 LT to 16:00 LT. The N_{CN} value increased under the low CS PNSD~~new background~~ scenario; however, the N_{CCN} barely changed, implying that larger size particles in the preexisting background play a more important role in scavenging newly-formed particles. We hence conclude that the newly-formed particles with a higher growth rate would grow faster to the CCN size by avoiding higher number concentration losses in the atmosphere (Fig. ~~S7a~~S9a). Our results highlight the importance of particle growth rate in modulating the N_{CCN} during NPF events.

It should be noted that the three NPF events discussed in this study were generally "Class I" regional NPF events, for which the growth rate and formation rate could be obtained with high confidence (Dal Maso et al., 2005). Other types (i.e., Class II proposed by Dal Maso et al. (2005)) were not considered since their growth rates and formation rates are extremely difficult to be determined, leading to high uncertainties in model simulation of these events. In addition, we did not include the "transport" type of NPF events, for which new particles were formed somewhere else and then transported to the measurement site, because the model ignores the impact of transport. Some events belonging to "Class II" type and "transport" type were observed during the campaign (Fig. S10). For the "Class II" type (Fig. S9 a), the number concentration and diameter of the nucleation and Aitken mode particles vary significantly. For the "transport" type (Fig. S10 b), the concentration of 3-30 nm particles at 10:00-12:00 LT was much lower than that of 30-70 nm at 12:00-20:00 LT, indicating the impact of transport. Investigation on the contribution of other NPF types to the N_{CCN} is needed in future studies. Moreover, this study only analyzed three NPF events as representatives of Class I type in the PRD region, and more field campaigns in other regions and seasons are also needed to identify the major impact factor.

4 Conclusions

Field measurements were conducted at a rural site in the PRD region of China during October and November 2019. The contribution of new particle formation (NPF) to the N_{CCN} was investigated based on three chosen NPF events including two (29th October and 18th November, 2019) from this field campaign and one (12th December, 2014) from a previous campaign in Panyu. The effects of several controlling factors on the contribution were explored to better understand the CCN activation process. These factors include formation rate, growth rate, background particle distribution, hygroscopicity and surface tension of the particles. Significant discrepancies were found for the κ values between measurements under supersaturation (using CCNc) and those under sub-saturation (using HTDMA), due partly to the pure water assumption for the surface tension when calculating the κ values based on the CCNc measurements. Organics in the particles could act as surfactants to lower the surface tension which facilitate CCN activation during NPF events. The results show that a surface tension value of about 0.060 N m^{-1} instead of 0.073 N m^{-1} (pure water assumption) could decrease the D_{50} (SS=1.0%) for 10 nm particles, bringing the agreement of the κ values between CCNc and HTDMA measurements. The surfactant effects caused by organics in the particles would increase the N_{CCN} at SS=1.0% by about 20% during non-event periods and by about 40% during NPF events. In addition, an earlier peak time was also observed because much higher number concentrations of small particles (3-100 nm) during the event would lead to smaller D_{50}.

The dynamic population balance equations were employed to qualitatively simulate NPF events under different case scenarios (coagulation term, formation term and growth term). Sensitivity studies were then performed to analyze the contribution of each aforementioned term to the N_{CCN}. The results

show that high formation rates, high growth rates, and low background particle concentrations lead to high total and CCN concentrations, although different mechanisms were attributed to the high N_{CN} and N_{CCN}. High formation rates lead to high particle production in the atmosphere; likewise, high growth rates produce a broad distribution of new particles and further increase the coagulation sources, while low background concentrations result in low coagulation scavenging with preexisting particles. Among these controlling factors, the growth rate was found to have the most ~~profound~~significant impact on the N_{CCN}, because a faster growth for newly-formed particles resulted in growing these particles to the CCN sizes in a shorter time before they were scavenged by preexisting particles. The N_{CCN} (SS=1.0%) measured from the chosen event on 12th December, 2014 was significantly lower than that from two other chosen events, initially attributed to the low growth rate, low formation rate, and low background particle concentration. Sensitivity tests were then performed under different scenarios (the highest growth rate form the event on 18th October, the highest formation rate and the lowest CS from the event on 29th October, respectively) with change of only one factor for each simulation. The results show that the peak value of the modeled N_{CCN} increased from 6000 to 14000 cm^{-3} with the new applied growth rate, leading to a similar value to that from the event on 18th October, while the modeled N_{CCN} values were barely affected under the two other scenarios. These results highlight the importance of the growth rate in the contribution of the controlling factors to the N_{CCN}. We concluded that surface tension and growth rate played a major role in the contribution of NPF event to the N_{CCN}. More work on the other NPF cases is obviously needed in order to better understand the contribution to the N_{CCN} and its impact on climate.

Data availability. Data from the measurements are available upon request (Bin Yuan via

byuan@jnu.edu.cn).

Supplement. The supplement related to this article is available online at xxx.

Author contributions. **MC, MS** and **BY** designed the research. **MC, MS, BY**, **SH, YP, ZW, DC, BL and QS** performed the measurements. **MC, BY, JZ, HT, FL, SH, HX, LL, YP, ZW, BL and QS** analyzed the data. **MC, BY** and **JZ** wrote the paper with contributions from all co-authors.

Competing interests. The authors declare that they have no conflict of interest.

Acknowledgements. This work was supported by the Key-Area Research and Development Program of Guangdong Province (grant No. 2019B110206001), the National Key R&D Plan of China (grant No. 2019YFE0106300, 2018YFC0213904), the National Natural Science Foundation of China (grant No. 41877302, 91644225, 41775117), Guangdong Natural Science Funds for Distinguished Young Scholar (grant No. 2018B030306037), Guangdong Innovative and Entrepreneurial Research Team Program (grant No. 2016ZT06N263), ~~and~~ Guangdong Province Key Laboratory for Climate Change and Natural Disaster Studies (Grant 2020B1212060025), Science and Technology Program of Guangdong Province (Science and Technology Innovation Platform Category, No.2019B121201002).

Reference

An, J., Wang, H., Shen, L., Zhu, B., Zou, J., Gao, J., and Kang, H.: Characteristics of new particle formation events in Nanjing, China: Effect of water-soluble ions, Atmos. Environ., 108, 32-40, https://doi.org/10.1016/j.atmosenv.2015.01.038, 2015.

Asmi, E., Frey, A., Virkkula, A., Ehn, M., Manninen, H., Timonen, H., Tolonen-Kivimäki, O., Aurela, M., Hillamo, R., and Kulmala, M.: Hygroscopicity and chemical composition of Antarctic sub-micrometre aerosol particles and observations of new particle formation, Atmos. Chem. Phys., 10, 4253-4271, 2010.

Bertram, A. K., Martin, S. T., Hanna, S. J., Smith, M. L., Bodsworth, A., Chen, Q., Kuwata, M., Liu, A., You, Y., and Zorn, S. R.: Predicting the relative humidities of liquid-liquid phase separation, efflorescence, and deliquescence of mixed particles of ammonium sulfate, organic material, and water using the organic-to-sulfate mass ratio of the particle and the oxygen-to-carbon elemental ratio of the organic component, Atmos. Chem. Phys., 11, 10995-11006, 10.5194/acp-11-10995-2011, 2011.

Boy, M., Kulmala, M., Ruuskanen, T. M., Pihlatie, M., Reissell, A., Aalto, P. P., Keronen, P., Dal Maso, M., Hellen, H., Hakola, H., Jansson, R., Hanke, M., and Arnold, F.: Sulphuric acid closure and contribution to nucleation mode particle growth, Atmos. Chem. Phys., 5, 863-878, 10.5194/acp-5-863-2005, 2005.

Cai, R., and Jiang, J.: A new balance formula to estimate new particle formation rate: reevaluating the effect of coagulation scavenging, Atmos. Chem. Phys., 17, 12659-12675, 10.5194/acp-17-12659-2017, 2017.

Cai, M., Tan, H., Chan, C. K., Qin, Y., Xu, H., Li, F., Schurman, M. I., Liu, L., and Zhao, J.: The size-resolved cloud condensation nuclei (CCN) activity and its prediction based on aerosol hygroscopicity and composition in the Pearl Delta River (PRD) region during wintertime 2014, Atmos. Chem. Phys., 18, 16419-16437, 2018.

Cai, M., Liang, B., Sun, Q., Zhou, S., Chen, X., Yuan, B., Shao, M., Tan, H., and Zhao, J.: Effects of continental emissions on cloud condensation nuclei (CCN) activity in the northern South China Sea

during summertime 2018, Atmos. Chem. Phys., 20, 9153-9167, 10.5194/acp-20-9153-2020, 2020.

Casquero-Vera, J. A., Lyamani, H., Dada, L., Hakala, S., Paasonen, P., Román, R., Fraile, R., Petäjä, T., Olmo-Reyes, F. J., and Alados-Arboledas, L.: New particle formation at urban and high-altitude remote sites in the south-eastern Iberian Peninsula, Atmos. Chem. Phys. Discuss., 2020, 1-32, 10.5194/acp-2020-394, 2020.

Chen, C., Hu, M., Wu, Z., Wu, Y., Guo, S., Chen, W., Luo, B., Zhang, Y., and Xie, S.: Characterization of new particle formation event in the rural site of Sichuan Basin and its contribution to cloud condensation nuclei, China Environ. Sci., 34, 2764-2772, 2014. (in Chinese)

Dal Maso, M., Kulmala, M., Riipinen, I., Wagner, R., Hussein, T., Aalto, P. P., and Lehtinen, K. E. J.: Formation and growth of fresh atmospheric aerosols: eight years of aerosol size distribution data from SMEAR II, Hyytiälä, Finland, Boreal Environ. Res., 10, 323-336, 2005.

Dameto de España, C., Wonaschütz, A., Steiner, G., Rosati, B., Demattio, A., Schuh, H., and Hitzenberger, R.: Long-term quantitative field study of New Particle Formation (NPF) events as a source of Cloud Condensation Nuclei (CCN) in the urban background of Vienna, Atmos. Environ., 164, 289-298, https://doi.org/10.1016/j.atmosenv.2017.06.001, 2017.

Deng, Y., Yai, H., Fujinari, H., Kawana, K., Nakayama, T., and Mochida, M.: Diurnal variation and size dependence of the hygroscopicity of organic aerosol at a forest site in Wakayama, Japan: their relationship to CCN concentrations, Atmos. Chem. Phys., 19, 5889-5903, 10.5194/acp-19-5889-2019, 2019.

Engelhart, G., Asa-Awuku, A., Nenes, A., and Pandis, S.: CCN activity and droplet growth kinetics of fresh and aged monoterpene secondary organic aerosol, Atmos. Chem. Phys., 8, 3937-3949, 2008.

Farmer, D. K., Cappa, C. D., and Kreidenweis, S. M.: Atmospheric Processes and Their Controlling Influence on Cloud Condensation Nuclei Activity, Chemical Reviews, 115, 4199, 2015.

Freedman, M. A.: Phase separation in organic aerosol, Chem. Soc. Rev., 46, 7694-7705, 10.1039/C6CS00783J, 2017.

Foucart, B., Sellegri, K., Tulet, P., Rose, C., Metzger, J. M., and Picard, D.: High occurrence of new particle formation events at the Maïdo high-altitude observatory (2150 m), Réunion (Indian Ocean), Atmos. Chem. Phys., 18, 9243-9261, 10.5194/acp-18-9243-2018, 2018.

765 Fuchs, N., and Sutugin, A.: High Dispersed Aerosols, Topics in Current Aerosol Research, in:
766 International Reviews in Aerosol Physics and Chemistry, Pergamon Press Oxford, 5-60, 1971.
767 Jiang, J., Zhao, J., Chen, M., Eisele, F. L., Scheckman, J., Williams, B. J., Kuang, C., and
768 McMurry, P. H.: First Measurements of Neutral Atmospheric Cluster and 1–2 nm Particle Number Size
769 Distributions During Nucleation Events, Aerosol Sci. Technol., 45, ii-v,
770 10.1080/02786826.2010.546817, 2011.
771 Kalkavouras, P., E. Bossioli, S. Bezantakos, A. Bougiatioti, N. Kalivitis, I. Stavroulas, G.
772 Kouvarakis, A. P. Protonotariou, A. Dandou, G. Biskos, N. Mihalopoulos, A. Nenes, & M. Tombrou
773 (2017), New particle formation in the southern Aegean Sea during the Etesians: importance for CCN
774 production and cloud droplet number, Atmos. Chem. Phys., 17(1), 175-192,
775 doi:10.5194/acp-17-175-2017.
776 Kuang, C., Chen, M., Zhao, J., Smith, J., McMurry, P. H., and Wang, J.: Size and time-resolved
777 growth rate measurements of 1 to 5 nm freshly formed atmospheric nuclei, Atmos. Chem. Phys., 12,
778 3573-3589, 10.5194/acp-12-3573-2012, 2012.
779 Kulmala, M., Vehkamäki, H., Petäjä, T., Dal Maso, M., Lauri, A., Kerminen, V. M., Birmili, W.,
780 and McMurry, P. H.: Formation and growth rates of ultrafine atmospheric particles: a review of
781 observations, J. Aerosol Sci., 35, 143-176, https://doi.org/10.1016/j.jaerosci.2003.10.003, 2004.
782 Kulmala, M., Petäjä, T., Nieminen, T., Sipilä, M., Manninen, H. E., Lehtipalo, K., Dal Maso, M.,
783 Aalto, P. P., Junninen, H., Paasonen, P., Riipinen, I., Lehtinen, K. E. J., Laaksonen, A., and Kerminen,
784 V.-M.: Measurement of the nucleation of atmospheric aerosol particles, Nature Protocols, 7, 1651,
785 10.1038/nprot.2012.091, 2012.
786 Kulmala, M., Petäjä, T., Mönkkönen, P., Koponen, I. K., Dal Maso, M., Aalto, P. P., Lehtinen, K.
787 E. J., and Kerminen, V. M.: On the growth of nucleation mode particles: source rates of condensable
788 vapor in polluted and clean environments, Atmos. Chem. Phys., 5, 409-416, 10.5194/acp-5-409-2005,
789 2005.
790 Lehtinen, K. E. J., and Kulmala, M.: A model for particle formation and growth in the atmosphere
791 with molecular resolution in size, Atmos. Chem. Phys., 3, 251-257, 10.5194/acp-3-251-2003, 2003.
792 Leng, C., Zhang, Q., Tao, J., Zhang, H., Zhang, D., Xu, C., Li, X., Kong, L., Cheng, T., and Zhang,
793 R.: Impacts of new particle formation on aerosol cloud condensation nuclei (CCN) activity in Shanghai:

case study, Atmos. Chem. Phys., 14, 11353-11365, 2014.

Liu, P., Song, M., Zhao, T., Gunthe, S. S., Ham, S., He, Y., Qin, Y. M., Gong, Z., Amorim, J. C., Bertram, A. K., and Martin, S. T.: Resolving the mechanisms of hygroscopic growth and cloud condensation nuclei activity for organic particulate matter, Nat. Commun., 9, 4076, 10.1038/s41467-018-06622-2, 2018.

Liu, P. F., Zhao, C. S., Göbel, T., Hallbauer, E., Nowak, A., Ran, L., Xu, W. Y., Deng, Z. Z., Ma, N., Mildenberger, K., Henning, S., Stratmann, F., and Wiedensohler, A.: Hygroscopic properties of aerosol particles at high relative humidity and their diurnal variations in the North China Plain, Atmos. Chem. Phys., 11, 3479-3494, 10.5194/acp-11-3479-2011, 2011.

Liu, S., Hu, M., Wu, Z., Wehner, B., Wiedensohler, A., and Cheng, Y.: Aerosol number size distribution and new particle formation at a rural/coastal site in Pearl River Delta (PRD) of China, Atmos. Environ., 42, 6275-6283, 2008.

Lu, Y., Yan, C., Fu, Y., Chen, Y., Liu, Y., Yang, G., Wang, Y., Bianchi, F., Chu, B., Zhou, Y., Yin, R., Baalbaki, R., Garmash, O., Deng, C., Wang, W., Liu, Y., Petäjä, T., Kerminen, V. M., Jiang, J., Kulmala, M., and Wang, L.: A proxy for atmospheric daytime gaseous sulfuric acid concentration in urban Beijing, Atmos. Chem. Phys., 19, 1971-1983, 10.5194/acp-19-1971-2019, 2019.

~~Liu, P. F., Zhao, C. S., Göbel, T., Hallbauer, E., Nowak, A., Ran, L., Xu, W. Y., Deng, Z. Z., Ma, N., Mildenberger, K., Henning, S., Stratmann, F., and Wiedensohler, A.: Hygroscopic properties of aerosol particles at high relative humidity and their diurnal variations in the North China Plain, Atmos. Chem. Phys., 11, 3479-3494, 10.5194/acp-11-3479-2011, 2011.~~

Ma, N., Zhao, C., Tao, J., Wu, Z., Kecorius, S., Wang, Z., Größ, J., Liu, H., Bian, Y., and Kuang, Y.: Variation of CCN activity during new particle formation events in the North China Plain, Atmos. Chem. Phys., 16, 8593-8607, 2016.

Ma, S. S., Chen, Z., Pang, S. F., and Zhang, Y. H.: Observations on hygroscopic growth and phase transitions of mixed 1, 2, 6-hexanetriol/$(NH_4)_2SO_4$ particles: Investigation of liquid-liquid phase separation (LLPS) dynamic process and mechanism and secondary LLPS, Atmos. Chem. Phys. Discuss., 2021, 1-18, 10.5194/acp-2020-1299, 2021.

Mikkonen, S., Romakkaniemi, S., Smith, J., Korhonen, H., Petäjä, T., Plass-Duelmer, C., Boy, M., McMurry, P., Lehtinen, K., and Joutsensaari, J.: A statistical proxy for sulphuric acid concentration, Atmos. Chem. Phys., 11, 11319-11334, 2011.

Mönkkönen, P., Koponen, I. K., Lehtinen, K. E. J., Hämeri, K., Uma, R., and Kulmala, M.: Measurements in a highly polluted Asian mega city: observations of aerosol number size distribution, modal parameters and nucleation events, Atmos. Chem. Phys., 5, 57-66, 10.5194/acp-5-57-2005, 2005.

Moore, R. H., Nenes, A., and Medina, J.: Scanning Mobility CCN Analysis—A Method for Fast Measurements of Size-Resolved CCN Distributions and Activation Kinetics, Aerosol Sci. Technol., 44, 861-871, 10.1080/02786826.2010.498715, 2010.

Nieminen, T., Lehtinen, K. E. J., and Kulmala, M.: Sub-10 nm particle growth by vapor condensation – effects of vapor molecule size and particle thermal speed, Atmos. Chem. Phys., 10, 9773-9779, 10.5194/acp-10-9773-2010, 2010.

Nieminen, T., Asmi, A., Dal Maso, M., Aalto, P. P., Keronen, P., Petäjä, T., Kulmala, M., and Kerminen, V.-M.: Trends in atmospheric new-particle formation: 16 years of observations in a boreal-forest environment, Boreal Environ. Res., 19 (suppl. B):191-214, 2014.

O'Dowd, C., McFiggans, G., Creasey, D. J., Pirjola, L., Hoell, C., Smith, M. H., Allan, B. J., Plane, J. M. C., Heard, D. E., Lee, J. D., Pilling, M. J., and Kulmala, M.: On the photochemical production of new particles in the coastal boundary layer, Geophys. Res. Lett., 26, 1707-1710, https://doi.org/10.1029/1999GL900335, 1999.

Ovadnevaite, J., Zuend, A., Laaksonen, A., Sanchez, K. J., Roberts, G., Ceburnis, D., Decesari, S., Rinaldi, M., Hodas, N., Facchini, M. C., Seinfeld, J. H., and O' Dowd, C.: Surface tension prevails over solute effect in organic-influenced cloud droplet activation, Nature, 546, 637-641, 10.1038/nature22806, 2017.

Paasonen, P., Nieminen, T., Asmi, E., Manninen, H. E., Petäjä, T., Plass-Dülmer, C., Flentje, H., Birmili, W., Wiedensohler, A., Hõrrak, U., Metzger, A., Hamed, A., Laaksonen, A., Facchini, M. C., Kerminen, V. M., and Kulmala, M.: On the roles of sulphuric acid and low-volatility organic vapours in the initial steps of atmospheric new particle formation, Atmos. Chem. Phys., 10, 11223-11242, 10.5194/acp-10-11223-2010, 2010.

Pajunoja, A., Lambe, A. T., Hakala, J., Rastak, N., Cummings, M. J., Brogan, J. F., Hao, L.,

Paramonov, M., Hong, J., and Prisle, N. L.: Adsorptive uptake of water by semisolid secondary organic aerosols, Geophys. Res. Lett., 42, 3063-3068, 2015.

~~Petäjä, T., Mauldin Iii, R., Kosciuch, E., McGrath, J., Nieminen, T., Paasonen, P., Boy, M., Adamov, A., Kotiaho, T., and Kulmala, M.: Sulfuric acid and OH concentrations in a boreal forest site, Atmos. Chem. Phys., 9, 7435-7448, 2009.~~

Petters, M., and Kreidenweis, S.: A single parameter representation of hygroscopic growth and cloud condensation nucleus activity, Atmos. Chem. Phys., 7, 1961-1971, 2007.

Rastak, N., A. Pajunoja, J. C. Acosta Navarro, J. Ma, M. Song, D. G. Partridge, A. Kirkevåg, Y. Leong, W. W. Hu, N. F. Taylor, A. Lambe, K. Cerully, A. Bougiatioti, P. Liu, R. Krejci, T. Petäjä, C. Percival, P. Davidovits, D. R. Worsnop, A. M. L. Ekman, A. Nenes, S. Martin, J. L. Jimenez, D. R. Collins, D. O. Topping, A. K. Bertram, A. Zuend, A. Virtanen, ~~&~~ and I. Riipinen~~ (2017),~~: Microphysical explanation of the RH-dependent water affinity of biogenic organic aerosol and its importance for climate, Geophys. Res. Lett., 44(10), 5167-5177, doi:10.1002/2017GL073056, 2017.~~

Renbaum-Wolff, L., Song, M., Marcolli, C., Zhang, Y., Liu, P. F., Grayson, J. W., Geiger, F. M., Martin, S. T., and Bertram, A. K.: Observations and implications of liquid–liquid phase separation at high relative humidities in secondary organic material produced by α-pinene ozonolysis without inorganic salts, Atmos. Chem. Phys., 16, 7969-7979, 10.5194/acp-16-7969-2016, 2016.

Rose, C., K. Sellegri, I. Moreno, F. Velarde, M. Ramonet, K. Weinhold, R. Krejci, M. Andrade, A. Wiedensohler, P. Ginot, ~~&~~and P. Laj~~ (2017);~~ CCN production by new particle formation in the free troposphere, Atmos. Chem. Phys., 17(2), 1529-1541, doi:10.5194/acp-17-1529-2017, 2017.~~

Ruehl, C. R., and Wilson, K. R.: Surface organic monolayers control the hygroscopic growth of submicrometer particles at high relative humidity, J. Phys. Chem. A, 118, 3952-3966, 2014.

Ruehl, C. R., Davies, J. F., and Wilson, K. R.: An interfacial mechanism for cloud droplet formation on organic aerosols, Science, 351, 1447-1450, 2016.

Shen, L., H. Wang, Y. Yin, J. Chen, and~~&~~ K. Chen~~ (2019);~~ Observation of atmospheric new particle growth events at the summit of mountain Tai (1534 m) in Central East China, Atmos. Environ., 201, 148-157, doi:https://doi.org/10.1016/j.atmosenv.2018.12.051, 2019.~~

Shen, X. J., J. Y. Sun, Y. M. Zhang, B. Wehner, A. Nowak, T. Tuch, X. C. Zhang, T. T. Wang, H. G. Zhou, X. L. Zhang, F. Dong, W. Birmili, ~~&~~and A. Wiedensohler~~ (2011),~~: First long-term study of

881 particle number size distributions and new particle formation events of regional aerosol in the North
882 China Plain, Atmos. Chem. Phys., 11(4), 1565-1580, doi:10.5194/acp-11-1565-2011~~.~~, 2011.
883 Spracklen, D. V., Carslaw, K. S., Kulmala, M., Kerminen, V. M., Sihto, S. L., Riipinen, I.,
884 Merikanto, J., Mann, G. W., Chipperfield, M. P., and Wiedensohler, A.: Contribution of particle
885 formation to global cloud condensation nuclei concentrations, J. Geophys. Res. Lett., 35, 2008.
886 Stocker, D. Q.: Climate change 2013: The physical science basis, Working Group I Contribution
887 to the Fifth Assessment Report of the Intergovernmental Panel on Climate Change, Summary for
888 Policymakers, IPCC, 2013.
889 Stolzenburg, M. R., and McMurry, P. H.: Equations Governing Single and Tandem DMA
890 Configurations and a New Lognormal Approximation to the Transfer Function, Aerosol Sci. Technol.,
891 42, 421-432, 10.1080/02786820802157823, 2008.
892 Tan, H., Xu, H., Wan, Q., Li, F., Deng, X., Chan, P. W., Xia, D., and Yin, Y.: Design and
893 Application of an Unattended Multifunctional H-TDMA System, J. Atmos. Oceanic Technol., 30,
894 1136-1148, 10.1175/JTECH-D-12-00129.1, 2013.
895 Topping, D. O., McFiggans, G. B., and Coe, H.: A curved multi-component aerosol hygroscopicity
896 model framework: Part 1 – Inorganic compounds, Atmos. Chem. Phys., 5, 1205-1222,
897 10.5194/acp-5-1205-2005, 2005.
898 ~~Vignati, E., Wilson, J., and Stier, P.: M7: An efficient size-resolved aerosol microphysics module~~
899 ~~for large-scale aerosol transport models, J. Geophys. Res. Lett., 109, 10.1029/2003jd004485, 2004.~~
900 Wang, S., Peng, Y., Qi, J., Wu, C., Wang, C., Wang, B., Wang, Z., Kuang, Y., Song, W., Wang, X.,
901 Hu, W., Chen, W., Shen, J., Chen, D., Shao, M., and Yuan, B.: Different chemical removal pathways of
902 volatile organic compounds (VOCs) s: Comparison of urban and regional sites, Acta Sci. Circumst., 40,
903 2311-2322, 2020. (in Chinese)
904 Wang, Z., Hu, M., Yue, D., He, L., Huang, X., Yang, Q., Zheng, J., Zhang, R., and Zhang, Y.: New
905 particle formation in the presence of a strong biomass burning episode at a downwind rural site in PRD,
906 China, Tellus B: Chem. Phys. Meteor., 65, 19965, 10.3402/tellusb.v65i0.19965, 2013.
907 ~~Wang, X., Jin, Y. G., Suto, M., Lee, L. C., and O'Neal, H. E.: Rate constant of the gas phase~~
908 ~~reaction of SO_3 with H_2O, J. Chem. Phys., 89, 4853-4860, 10.1063/1.455680, 1988.~~
909 ~~Wang, Z., Hu, M., Yue, D., He, L., Huang, X., Yang, Q., Zheng, J., Zhang, R., and Zhang, Y.: New~~

particle formation in the presence of a strong biomass burning episode at a downwind rural site in PRD, China, Tellus B: Chem. Phys. Meteor., 65, 19965, 10.3402/tellusb.v65i0.19965, 2013.

Wex, H., M. D. Petters, C. M. Carrico, E. Hallbauer, A. Massling, G. R. McMeeking, L. Poulain, Z. Wu, S. M. Kreidenweis, & F. Stratmann (2009), Towards closing the gap between hygroscopic growth and activation for secondary organic aerosol: Part 1 – Evidence from measurements, Atmos. Chem. Phys., 9(12), 3987-3997, doi:10.5194/acp-9-3987-2009.

Wolfe, G. M., Marvin, M. R., Roberts, S. J., Travis, K. R., and Liao, J.: The Framework for 0-D Atmospheric Modeling (F0AM) v3.1, Geosci. Model Dev., 9, 3309-3319, 10.5194/gmd-9-3309-2016, 2016.

Wu, Z., Hu, M., Liu, S., Wehner, B., Bauer, S., Ma ßling, A., Wiedensohler, A., Petäjä, T., Dal Maso, M., and Kulmala, M.: New particle formation in Beijing, China: Statistical analysis of a 1-year data set, J. Geophys. Res., 112, D09209, 10.1029/2006jd007406, 2007.

Wu, Z., Birmili, W., Poulain, L., Wang, Z., Merkel, M., Fahlbusch, B., Pinxteren, D. v., Herrmann, H., and Wiedensohler, A.: Particle hygroscopicity during atmospheric new particle formation events: implications for the chemical species contributing to particle growth, Atmos. Chem. Phys., 13, 6637-6646, 2013a.

Wu, Z., Poulain, L., Henning, S., and Dieckmann, K.: Relating particle hygroscopicity and CCN activity to chemical composition during the HCCT-2010 field campaign, Atmos. Chem. Phys., 13, 7983-7996, 2013b.

Yu, H., Ortega, J., Smith, J. N., Guenther, A. B., Kanawade, V. P., You, Y., Liu, Y., Hosman, K., Karl, T., Seco, R., Geron, C., Pallardy, S. G., Gu, L., Mikkilä, J., and Lee, S.-H.: New Particle Formation and Growth in an Isoprene-Dominated Ozark Forest: From Sub-5 nm to CCN-Active Sizes, Aerosol Sci. Technol., 48, 1285-1298, 10.1080/02786826.2014.984801, 2014.

Yue, D., Zhong, L., Zhang, T., Shen, J., Yuan, L., Ye, S., Zhou, Y., and Zeng, L.: Particle growth and variation of cloud condensation nucleus activity on polluted days with new particle formation: A case study for regional air pollution in the PRD region, China, Aerosol Air Qual. Res., 16, 323-335, 2016.

Yue, D. L., Hu, M., Zhang, R. Y., Wu, Z. J., Su, H., Wang, Z. B., Peng, J. F., He, L. Y., Huang, X. F., Gong, Y. G., and Wiedensohler, A.: Potential contribution of new particle formation to cloud

condensation nuclei in Beijing, Atmos. Environ., 45, 6070-6077, https://doi.org/10.1016/j.atmosenv.2011.07.037, 2011.

Yue, D. L., Hu, M., Wang, Z. B., Wen, M. T., Guo, S., Zhong, L. J., Wiedensohler, A., and Zhang, Y. H.: Comparison of particle number size distributions and new particle formation between the urban and rural sites in the PRD region, China, Atmos. Environ., 76, 181-188, https://doi.org/10.1016/j.atmosenv.2012.11.018, 2013.

946 FIGURE CAPTIONS

947 Figure 1. The PNSD (a), N_{CN}, N_{CCN} and AR (b), wind speed and wind direction (c), $j_{O(1D)}$, and
948 concentration of calculated H_2SO_4 (d) during the NPF event on 29th October, 2019. The blue dots in (a)
949 represents the geometric mean particle diameter (Dp_{gmd}) and the red line represents the linear fitting.

950 Figure 2. Comparison of the median and interquartile κ values obtained from HTDMA and CCN
951 measurements during this campaign at Heshan, at Panyu (urban Guangzhou), and from South China
952 Sea. The κ was pointed against the corresponding median D_{50} (CCN measurement) or selected diameter
953 (HTDMA measurement). Dots represent the median values and bars represent the interquartile ranges.
954 The κ values in this measurement were obtained from HTDMA measurement (in black) and CCNc
955 measurement (ss=0.1%, 0.2%, 0.4%, 0.7%, 0.9%, and 1.0% in red and yellow for different surface
956 tensions). The yellow lines and dots represent the κ values recalculated based on $\sigma_{s/a}^*$. The κ values at
957 Panyu were obtained from HTDMA measurement (in purple) and CCNc measurement (ss=0.1%, 0.2%,
958 0.4%, and 0.7%, in green). The κ values from the South China Sea were obtained from CCNc
959 measurement (ss=0.18%, 0.34%, and 0.59%, in light blue). The κ values from the North China Plain
960 were obtained from HTDMA measurement.

961 ~~Figure 2. The median and interquartile κ obtained from HTDMA and CCN measurements during this~~
962 ~~campaign, at the Panyu site (urban Guangzhou), and from South China Sea. The κ was pointed against~~
963 ~~the corresponding median D_{50} (CCN measurement) or selected diameter (HTDMA measurement). Dots~~
964 ~~represent the median values and bars represent the interquartile ranges. The κ values in this~~
965 ~~measurement were obtained from HTDMA measurement (in bule) and CCNc measurement (ss=0.1%,~~
966 ~~0.2%, 0.4%, 0.7%, 0.9%, and 1.0% in red and yellow for different surface tensions). The yellow lines~~
967 ~~and dots represent the κ values recalculated based on $\sigma^{s/a*}$. The κ values in the Panyu measurement~~

~~were obtained from HTDMA measurement (in purple) and CCNc measurement (ss=0.1%, 0.2%, 0.4%, and 0.7%, in green). The κ values from the South China Sea were obtained from CCNc measurement (ss=0.18%, 0.34%, and 0.59%, in light blue). The κ values from the North China Plain were obtained from HTDMA measurement.~~

Figure 3. The variation of Dp_{gmd} (blue dots), $D_{50,m}$ ~~measured D_{50}~~ (yellow dots) and $D_{50,r}$ ~~recalculated D_{50}~~ (red dots) based on pure water surface tension.

Figure 4. The variation of N_{CCN} (a), activation ratio(b), and δ_{CCN} (c) based on the $D_{50,m}$ ~~measured D_{50}~~, the $D_{50,r}$ ~~recalculated D_{50}~~, and the average D_{50}. The red line represents the measured values. The yellow line represents the values calculated based on the surface tension of pure water (0.072 N m^{-1}). The purple line represents the values calculated from the average D_{50}. The green region represents the interquartile values calculated from the interquartile D_{50}.

Figure. 5 The measured and model PNSD (a and b), N_{CN} (c) and N_{CCN} (c). The blue lines in (c) represent the measured values and the red lines represent the model values.

Figure 6. The variation of measured and model N_{CN} (a) and N_{CCN} (b) at 1.0% SS. The simulations was based on standard characteristic (red solid line), halving of GR, formation rate and background particle distribution (orange, purple and green solid line, respectively) and doubling of GR, formation rate and background particle distribution (orange, purple and green dash line, respectively).

Figure 7. The number contribution (a) and its fraction (b) of CoagSnk term, CoagSrc term, GR term, and formation (J) term to the N_{CCN} when it reached its peak value based under different case scenarios.

Figure. 8 The model N_{CCN} based on different characteristics (doubling growth rate and formation rate, and halfling background particle distribution) and particle properties. Different colors and markers represent case 1-9, respectively.

Figure ~~8~~9. The measured PNSD (a, b, and c), model PNSD (d, e, and f), measured N_{CN} and model N_{CN} (g, h, and i) during different NPF events. Solid and dash lines represent the measured and model N_{CN}, respectively.

Figure ~~9~~10. The measured and model N_{CCN} (SS=1.0%) during different NPF events.

Figure 1~~0~~1. The measured and model N_{CN} (a) and N_{CCN} (b) on the Panyu NPF event. The bule line represents the measured value. The red, yellow, purple and green lines represent the simulated N_{CCN} based on standard input, growth rate of the NPF event on October 18th (refer as high GR), formation rate of the NPF event on October 29th (refer as high J), and new background particle distribution of the NPF event on October 29th (refer as low CS PNSD), respectively.

1000

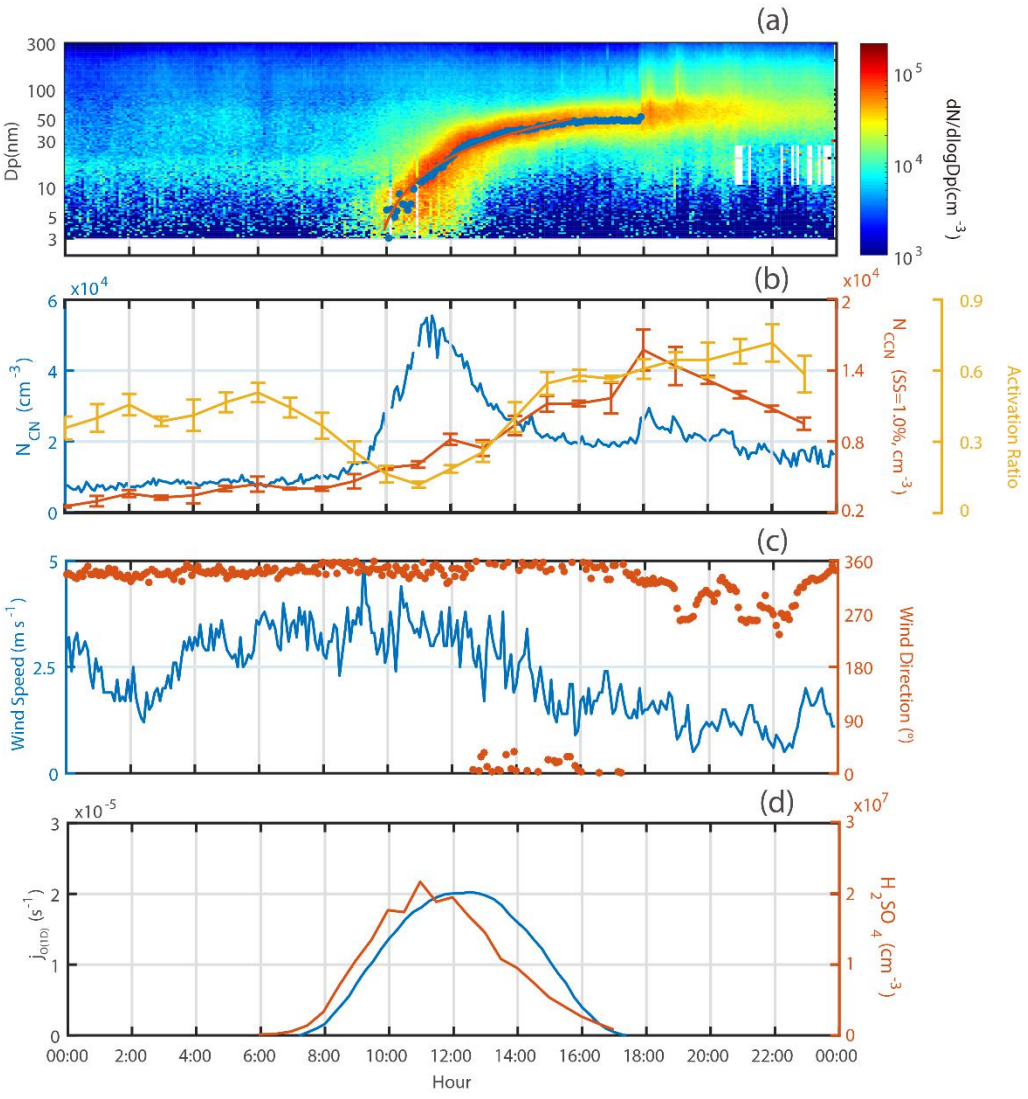
(a)
Dp(nm)
300
100
50
30
10
5
3
dN/dlogDp(cm-3)
10^5
10^4
10^3
(b)
x10^4
N_CN (cm-3)
N_CCN (SS=1.0%, cm-3)
Activation Ratio
(c)
Wind Speed (m s-1)
Wind Direction (°)
(d)
x10^-5
x10^7
j_O(1D) (s-1)
H2SO4 (cm-3)
00:00
2:00
4:00
6:00
8:00
10:00
12:00
14:00
16:00
18:00
20:00
22:00
00:00
Hour

1001

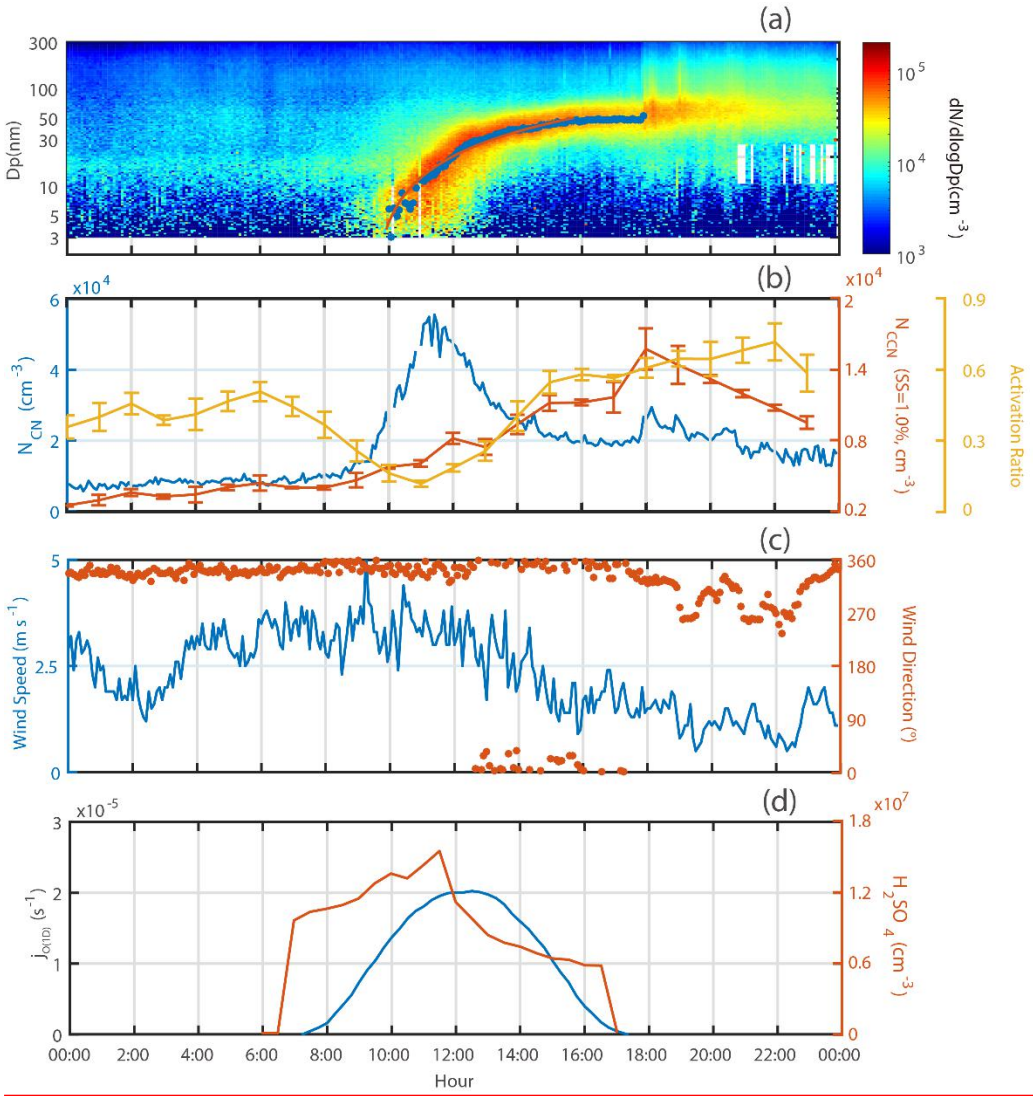

1002

1003 Fig. 1.

1004

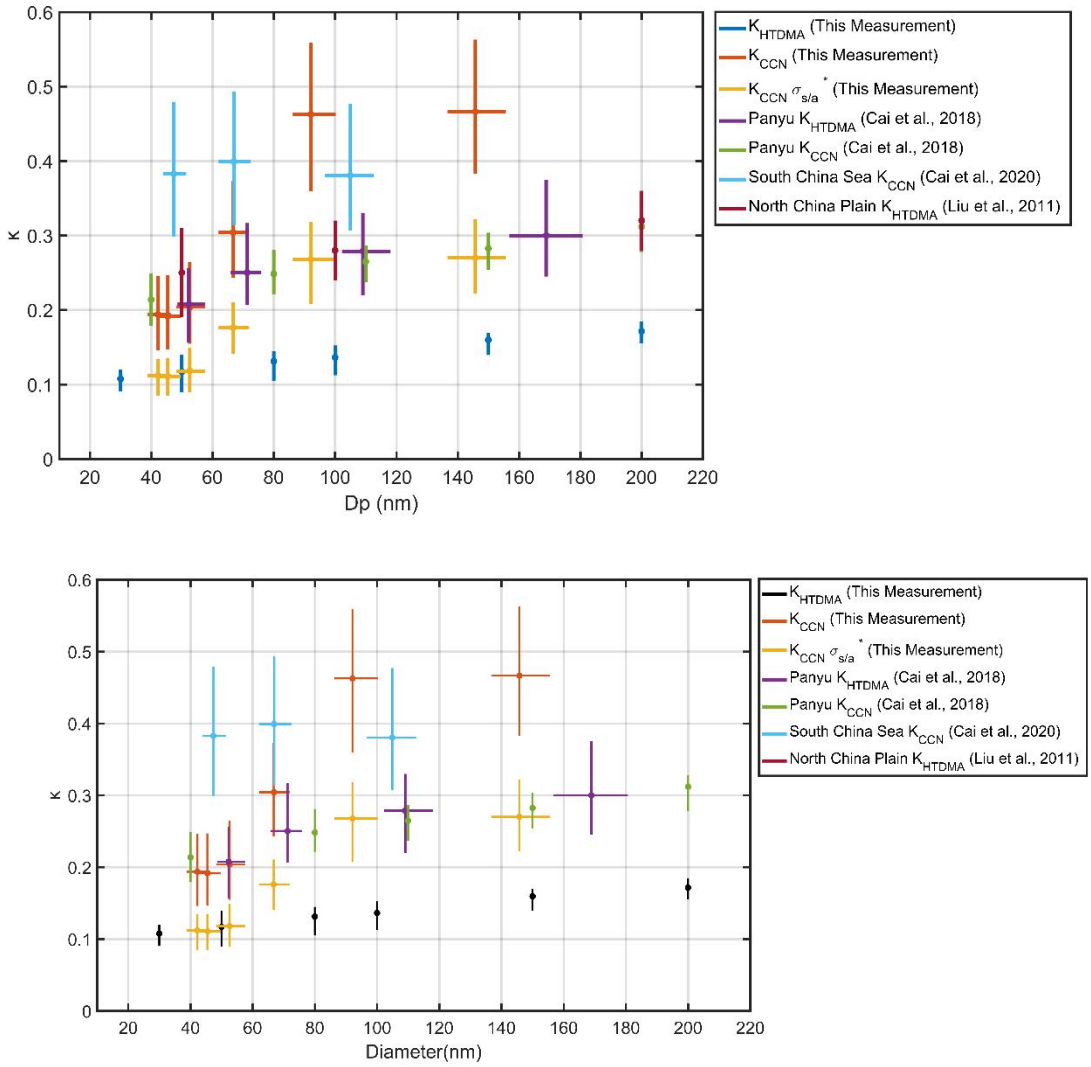
κ
Dp (nm)
Diameter(nm)
K_HTDMA (This Measurement)
K_CCN (This Measurement)
K_CCN σ_s/a* (This Measurement)
Panyu K_HTDMA (Cai et al., 2018)
Panyu K_CCN (Cai et al., 2018)
South China Sea K_CCN (Cai et al., 2020)
North China Plain K_HTDMA (Liu et al., 2011)

Fig. 2.

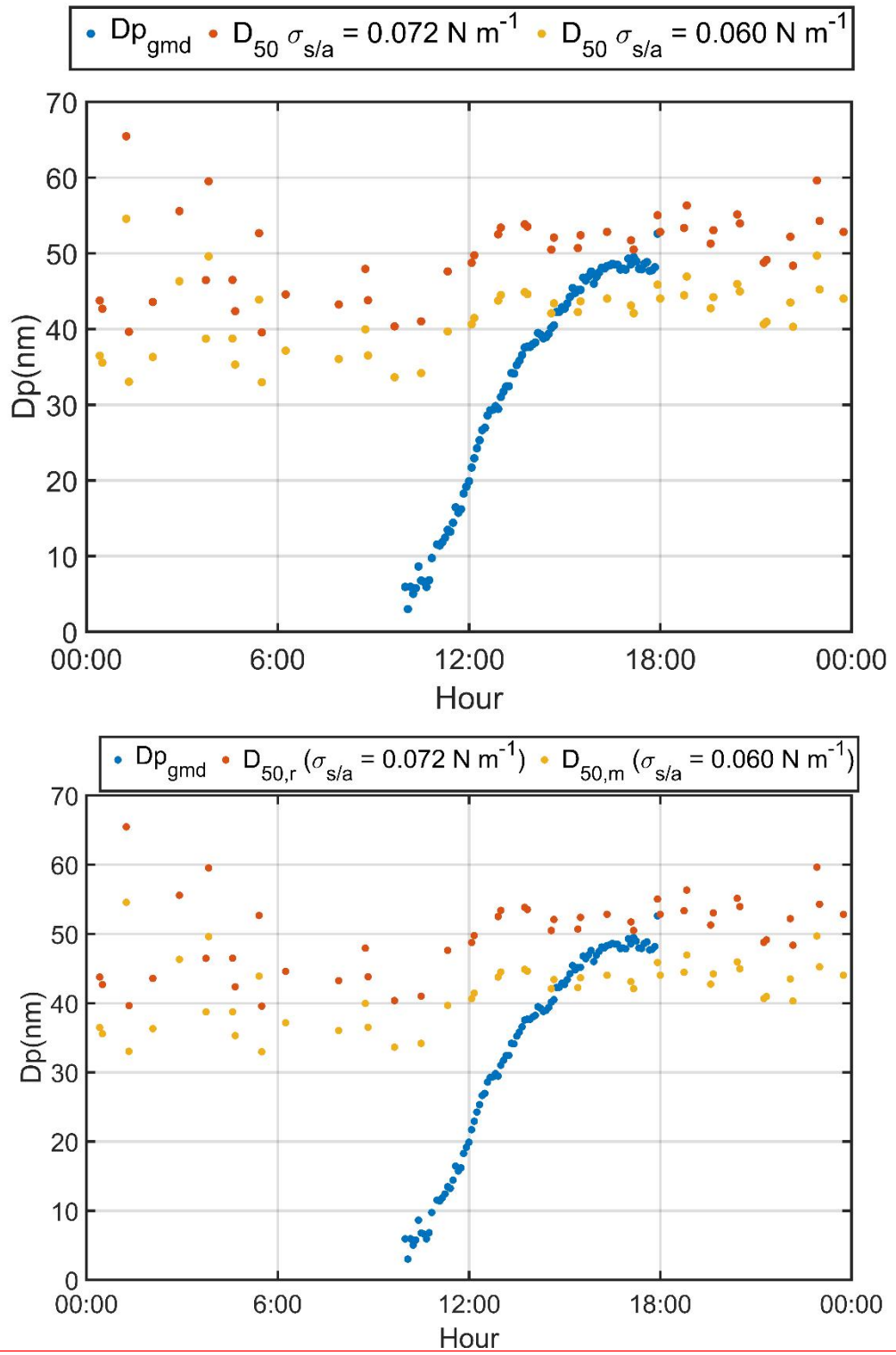
Dp_gmd
D50 σs/a = 0.072 N m-1
D50 σs/a = 0.060 N m-1
Dp(nm)
Hour
00:00
6:00
12:00
18:00
00:00
Dp_gmd
D50,r (σs/a = 0.072 N m-1)
D50,m (σs/a = 0.060 N m-1)
Dp(nm)
Hour

Fig. 3.

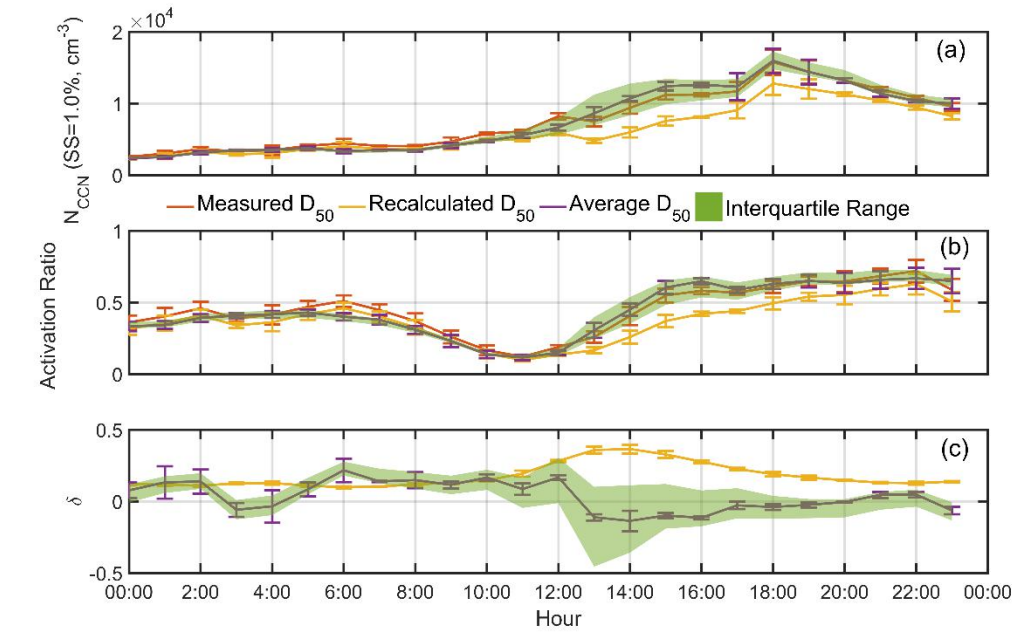

1014

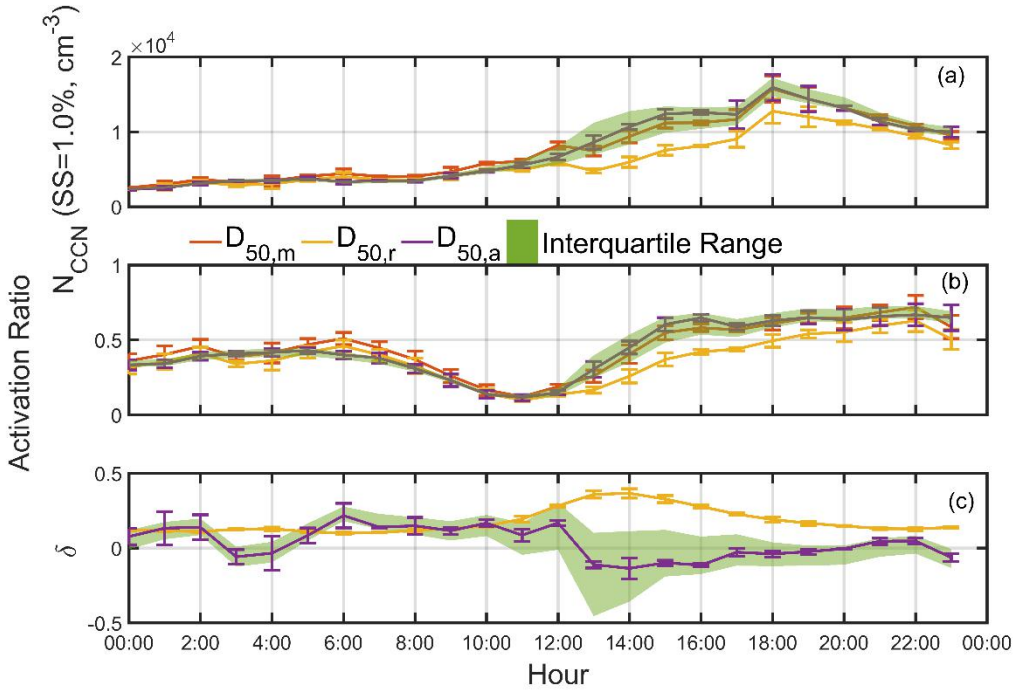

1015

1016

1017 Fig. 4.

1018

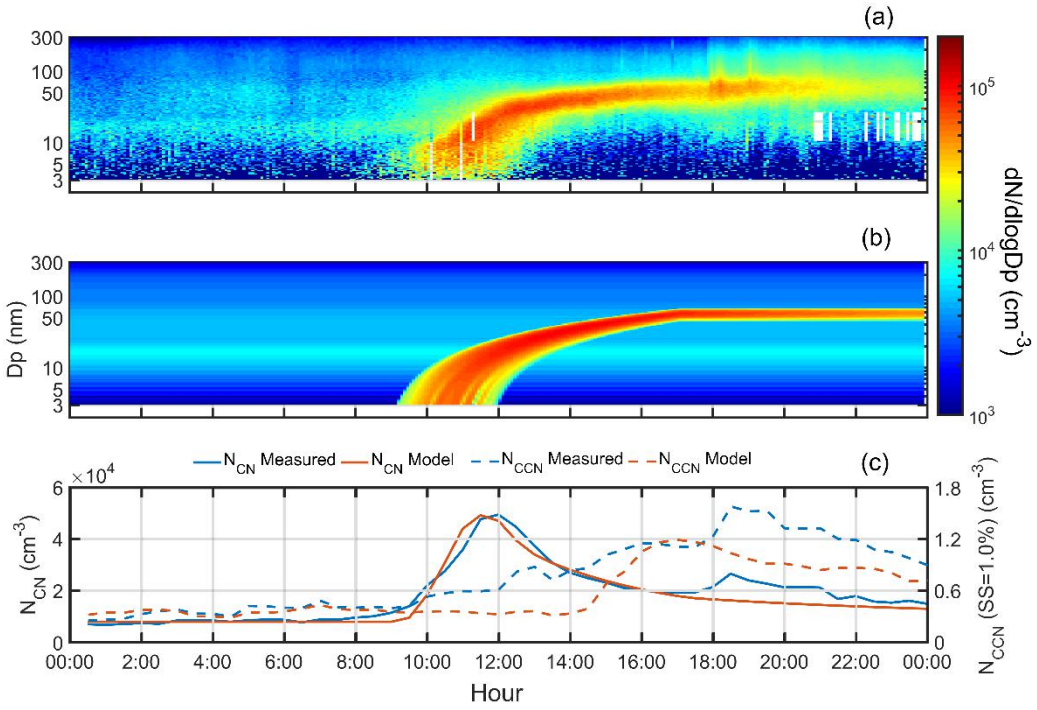

1019

1020

1021 Fig. 5.

1022

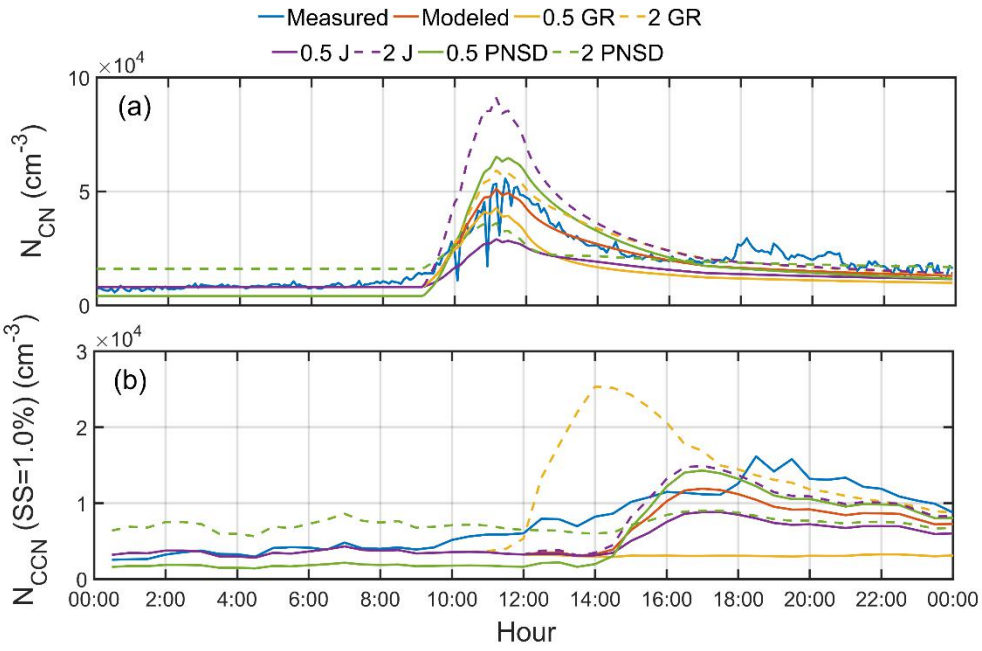

1023

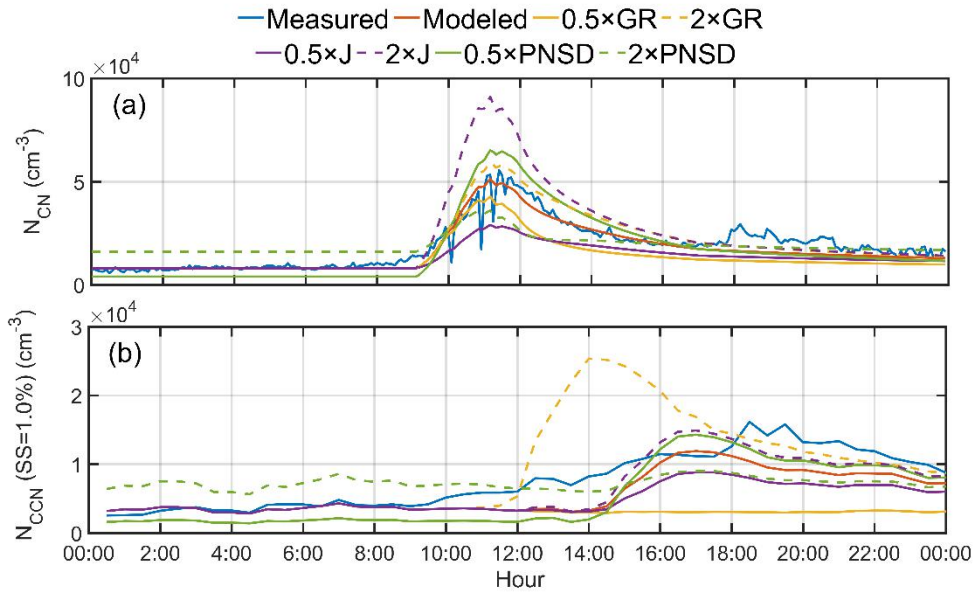

1024

1025

1026 Fig. 6.

1027

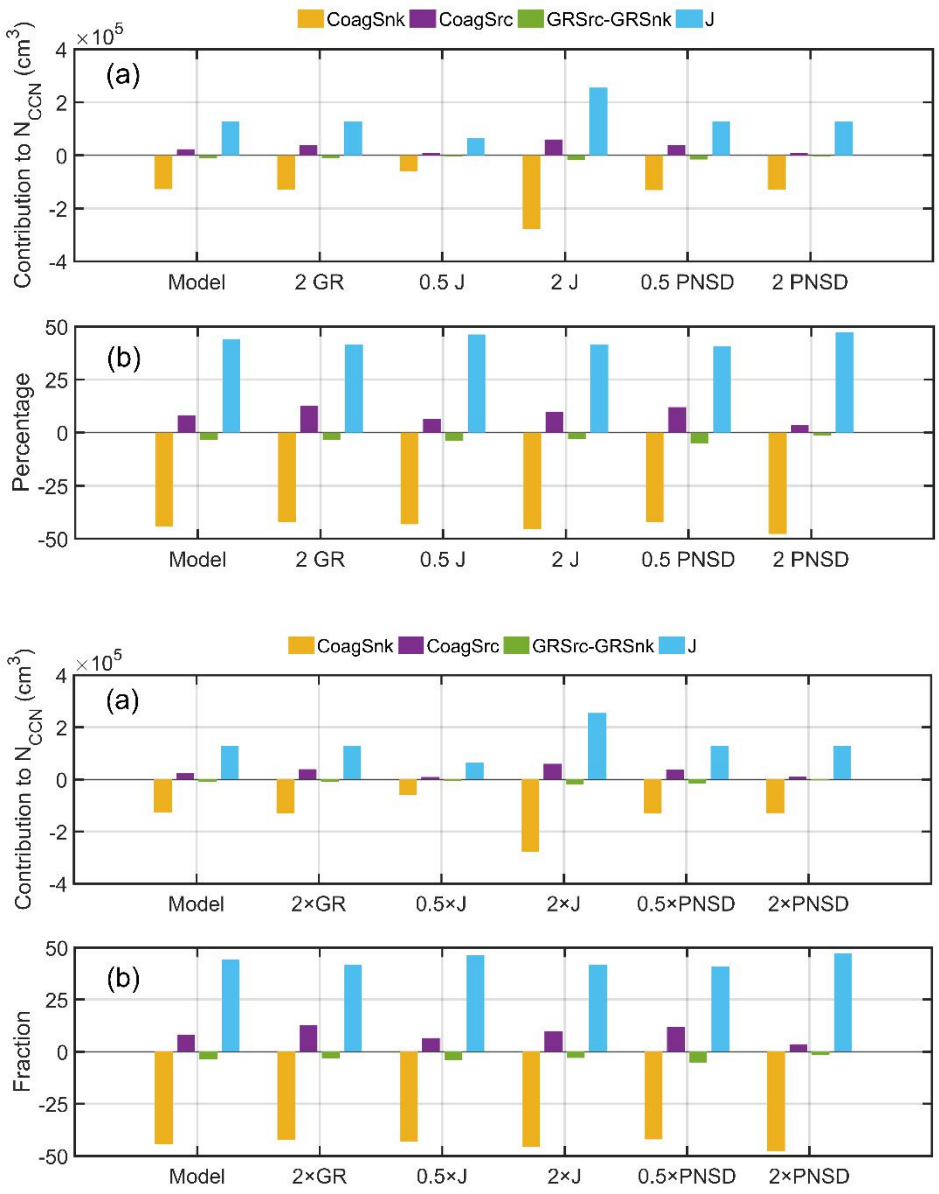
CoagSnk
CoagSrc
GRSrc-GRSnk
J
(a)
Contribution to N_{CCN} (cm^3)
$\times 10^5$
4
2
0
-2
-4
Model
2 GR
0.5 J
2 J
0.5 PNSD
2 PNSD
(b)
Percentage
50
25
0
-25
-50
Model
2 GR
0.5 J
2 J
0.5 PNSD
2 PNSD
CoagSnk
CoagSrc
GRSrc-GRSnk
J
(a)
Contribution to N_{CCN} (cm^3)
$\times 10^5$
4
2
0
-2
-4
Model
2×GR
0.5×J
2×J
0.5×PNSD
2×PNSD
(b)
Fraction
50
25
0
-25
-50
Model
2×GR
0.5×J
2×J
0.5×PNSD
2×PNSD

Fig. 7.

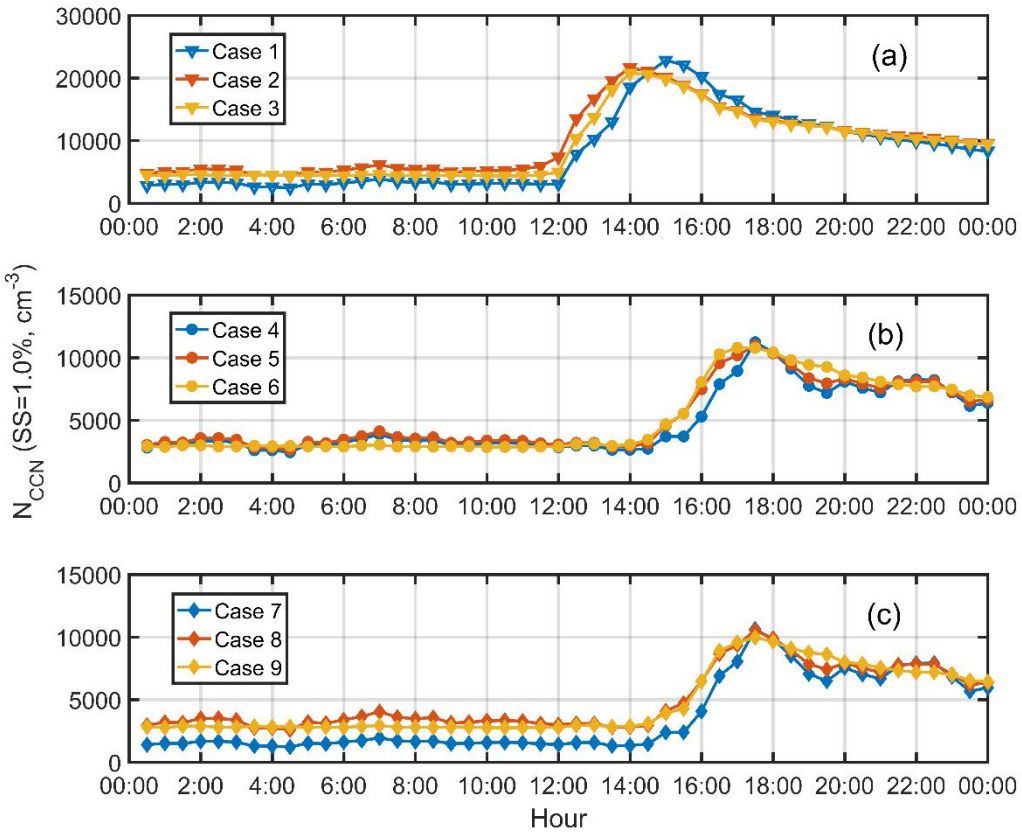
30000
20000
10000
0
Case 1
Case 2
Case 3
(a)
00:00 2:00 4:00 6:00 8:00 10:00 12:00 14:00 16:00 18:00 20:00 22:00 00:00
15000
10000
5000
0
Case 4
Case 5
Case 6
(b)
00:00 2:00 4:00 6:00 8:00 10:00 12:00 14:00 16:00 18:00 20:00 22:00 00:00
15000
10000
5000
0
Case 7
Case 8
Case 9
(c)
00:00 2:00 4:00 6:00 8:00 10:00 12:00 14:00 16:00 18:00 20:00 22:00 00:00
Hour
N_CCN (SS=1.0%, cm^-3)

Fig. 8

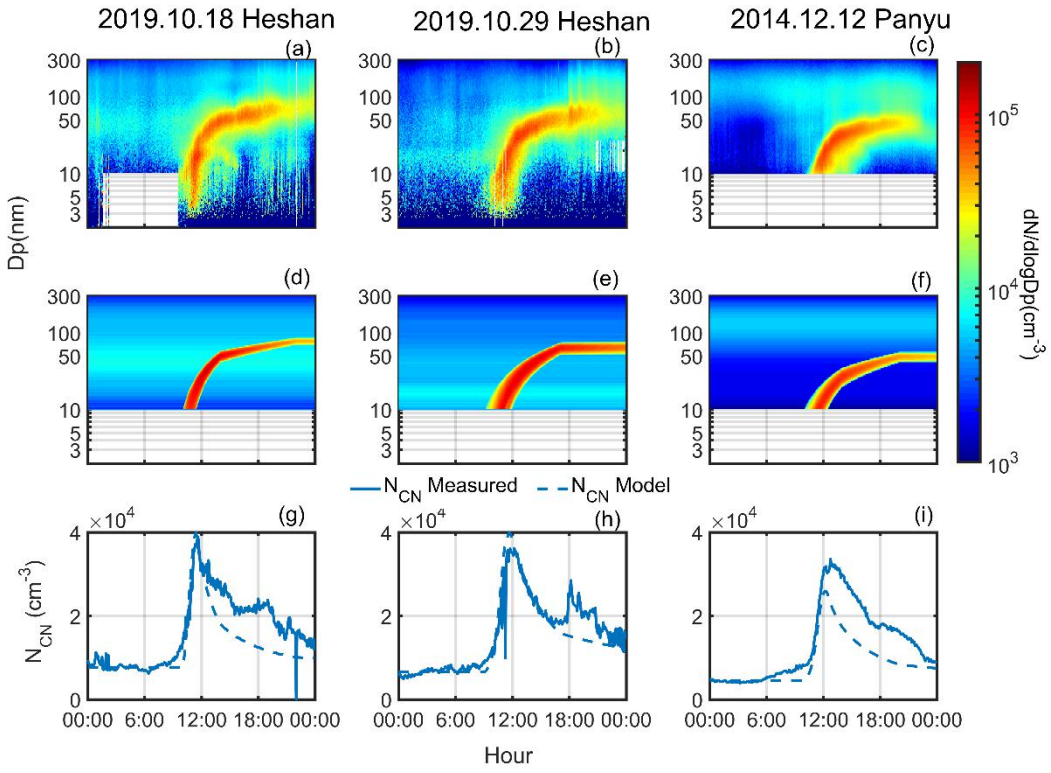
2019.10.18 Heshan
2019.10.29 Heshan
2014.12.12 Panyu
(a)
(b)
(c)
(d)
(e)
(f)
(g)
(h)
(i)
Dp(nm)
300
100
50
10
5
3
dN/dlogDp(cm-3)
10^5
10^4
10^3
N_CN Measured
N_CN Model
N_CN (cm-3)
×10^4
4
2
0
00:00 6:00 12:00 18:00 00:00
Hour

Fig. ~~8~~9.

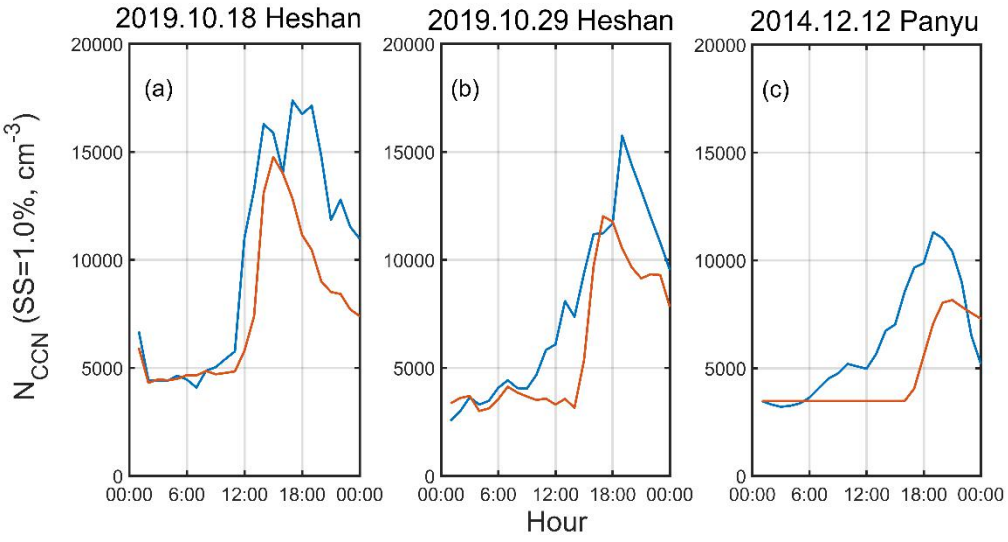

1042

1043

1044 Fig. 910.

1045

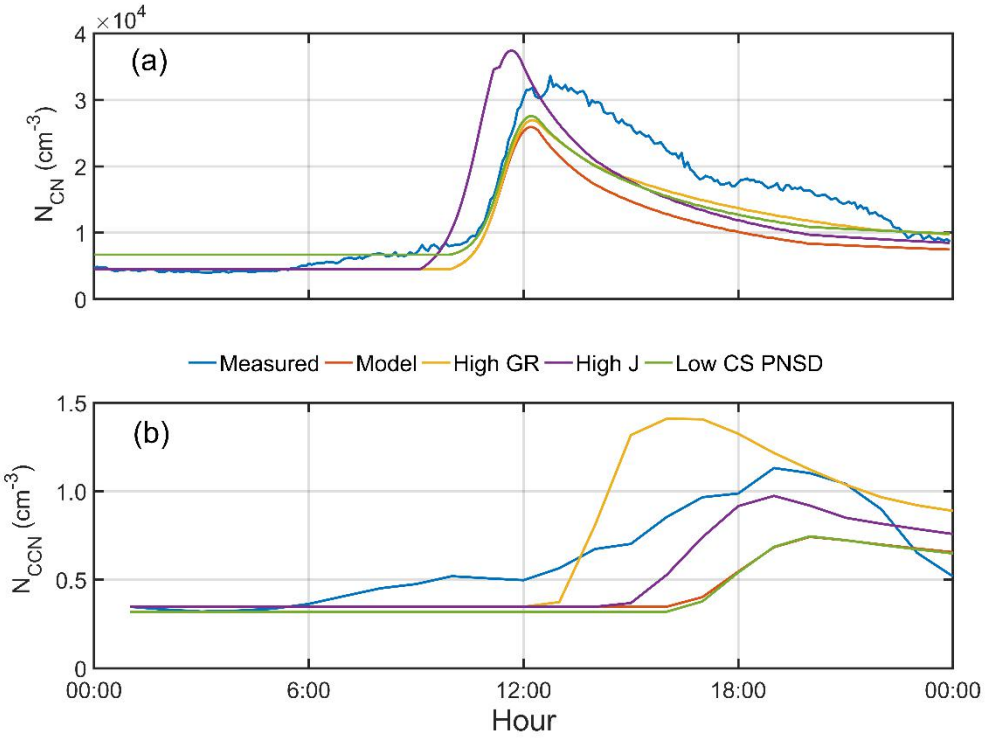
×10^4
(a)
N_CN (cm^-3)
Measured
Model
High GR
High J
Low CS PNSD
(b)
N_CCN (cm^-3)
00:00
6:00
12:00
18:00
00:00
Hour

Fig. 11.

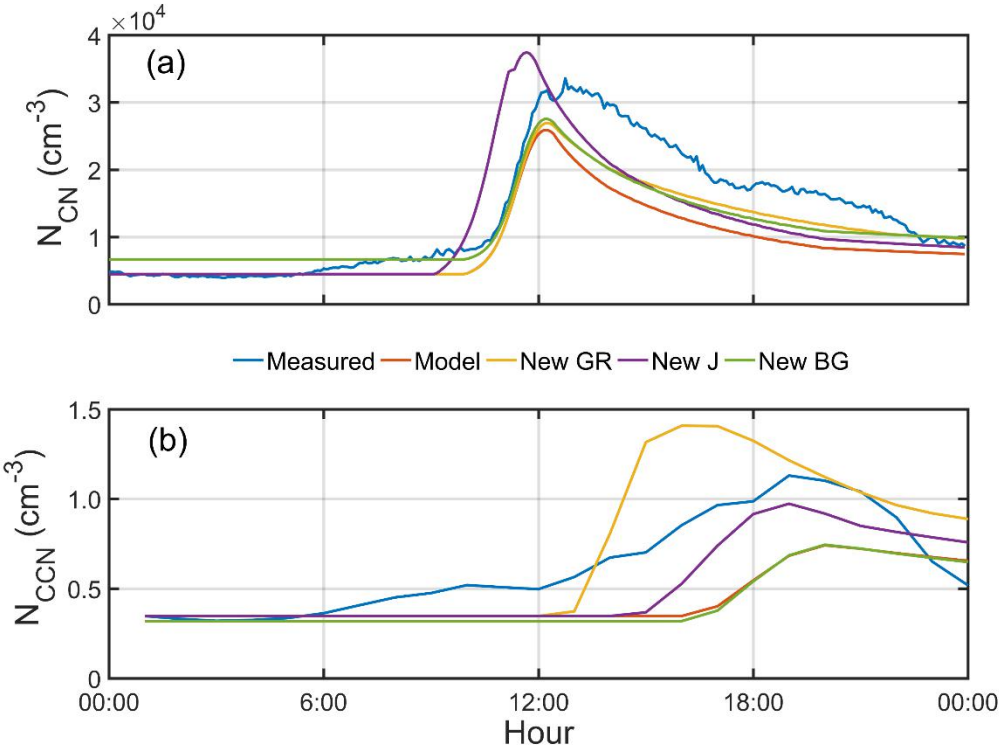
×10^4
(a)
N_CN (cm^-3)
Measured
Model
New GR
New J
New BG
(b)
N_CCN (cm^-3)
00:00
6:00
12:00
18:00
00:00
Hour

~~Fig. 10.~~

–